The Astrophysical Journal, 969:115 (18pp), 2024 July 10 https://doi.org/10.3847/1538-4357/ad47f8

A Rare, Strong Shock Front in the Merging Cluster SPT-CLJ 2031-4037

Purva Diwanji, Stephen A. Walker, and M. S. Mirakhor
Department of Physics and Astronomy, The University of Alabama in Huntsville, 301 Sparkman Drive NW, Huntsville, AL 35899, USA

Received 2023 June 27; revised 2024 April 11; accepted 2024 May 5; published 2024 July 4

Abstract

We present our findings from the new deep Chandra observations (256 ks) of the merging galaxy cluster SPT-CLJ 2031-4037 at $z = 0.34$. Our observations reveal intricate structures seen in a major merger akin to the Bullet Cluster. The X-ray data confirm the existence of two shock fronts, one to the northwest and one to the southeast, by directly measuring the temperature jump of gas across the surface brightness edges. The stronger shock front in the northwest has a density jump of 3.16 ± 0.34 across the sharp surface brightness edge and Mach number $M = 3.36^{+0.87}_{-0.48}$, which makes this cluster one of the rare merging systems with a Mach number $M > 2$. We use the northwestern shock to compare two models for shock heating—the instant heating model and the Coulomb collisional heating model—and we determine that the temperatures across the shock front agree with the Coulomb collisional model of heating. For the shock front in the southeastern region, we find a density jump of 1.53 ± 0.14 and a Mach number of $M = 1.36^{+0.09}_{-0.08}$.

Unified Astronomy Thesaurus concepts: Galaxy clusters (584); Shocks (2086); X-ray astronomy (1810); Intracluster medium (858)

1. Introduction

Galaxy clusters, the most massive gravitationally bound structures in the Universe, are formed through hierarchical mergers of smaller subclusters (Dasadia et al. 2016). Mergers of galaxy clusters are the most energetic events in the Universe after the Big Bang wherein the subclusters collide at velocities of $\sim 10^3$ km s^{-1}, releasing energy of the order of 10^{64} erg (Sarazin 2002). A fraction of the kinetic energy released during mergers is dissipated into the intracluster medium (ICM) via shocks and turbulence and may also cause nonthermal phenomena such as amplification of magnetic fields in the ICM and acceleration of ultrarelativistic particles in the cluster (Blandford & Eichler 1987; Sarazin 2008).

Shock fronts, seen as sharp discontinuities in X-ray brightness and temperature, provide a rare chance to observe and investigate such merger systems and their geometry. They are also used to measure gas bulk velocities and to understand transport processes in the ICM, including electron–ion equilibration and thermal conduction, magnetic fields, and turbulence (Takizawa 1999; Markevitch & Vikhlinin 2007).

SPT-CLJ 2031-4037 (hereafter SPT J2031) is a massive merger system with $M_{500} \sim 8 \times 10^{14}\, M_{\odot}$ (Chiu et al. 2018) and X-ray luminosity $L_{[0.1-2.4\mathrm{keV}]} = 1.04 \times 10^{45}$ erg s^{-1} (Piffaretti et al. 2011) at redshift $z = 0.34$ (Böhringer et al. 2004). The morphologically disturbed cluster (Nurgaliev et al. 2017) was first discovered in a ROSAT-ESO Flux Limited X-ray (REFLEX) galaxy cluster survey (Böhringer et al. 2004) as RXCJ2031.8-4037. It was also cataloged via the Sunyaev–Zel'dovich effect by the South Pole Telescope (SPT; Plagge et al. 2010; Williamson et al. 2011) and the Planck Satellite (Planck Collaboration et al. 2016). The redshift of this system is similar to that of the Bullet Cluster (redshift $z = 0.3$), and hence the size of their angular features are comparable.

A previous 10 ks Chandra observation revealed two surface brightness peaks indicating that it is very likely a major merger. Recent radio observations of SPT J2031 performed with the GMRT at 325 MHz and with the Very Large Array (*L*-band observation) at 1.7 GHz revealed diffuse radio emission in the cluster (Raja et al. 2020) leading to the speculation of a merger event in the past, which can be confirmed with deep X-ray observations. To investigate the possible occurrence of a shock front, we obtained deep Chandra observations.

In this paper, we present our results from deep Chandra observations of SPT J2031, which include the detection of a strong merger shock, a spatially resolved temperature map, and the preferred method of shock heating. In Section 2 we outline details of the observations and discuss the data reduction. In Sections 3 and 4 we present an image analysis and show the emissivity, temperature map, pseudopressure map, and a Gaussian gradient magnitude (GGM)-filtered image. In Section 5, we analyze the primary shock and the southeastern edge in more detail by obtaining surface brightness profiles and temperature profiles. Understanding the process of electron–ion equilibration is crucial in deciphering the complex dynamics of shock fronts in merging galaxy clusters. In this paper, we present a comprehensive analysis of an electron–ion equilibration test performed on the shock fronts observed in the galaxy cluster SPT J2031. The investigation involves the comparison of two prominent models of shock heating: an adiabatic-collisional model and an instant shock-heating model. The postshock electron temperature profiles are compared to the Coulomb collisional and instant shock-heating models for electron–ion equilibration.

We assume a flat cosmology with $H_0 = 70$ km s^{-1} Mpc^{-1}, $\Omega_{\mathrm{m}} = 0.3$, and $\Omega_{\Lambda} = 0.7$. The redshift is $z = 0.34$ where $1''$ corresponds to 4.892 kpc. All the error bars are at the 68% confidence level unless stated otherwise.

2. Chandra Data Analysis

SPT J2031 was observed by the Chandra Advanced CCD Imaging Spectrometer (ACIS) detector in the Very Faint mode

Table 1
Details of the Deep (∼250 ks) Chandra Observations of the SPT J2031 Cluster Utilized for the Analysis Shown in This Paper

ObsID	R.A.	Decl.	Date	Exp. Time (ks)	Cleaned Time (ks)
21539	20 31 51.10	−40 37 22.10	2019 Aug 05	36.0	32.8
24505	20 31 51.64	−40 37 19.64	2021 Aug 04	29.7	27.6
24508	20 31 51.64	−40 37 19.64	2021 Aug 09	27.7	26.4
24510	20 31 51.64	−40 37 19.64	2021 Aug 23	22.75	20.7
24509	20 31 51.64	−40 37 19.64	2021 Aug 28	32.6	30.6
24507	20 31 51.64	−40 37 19.64	2021 Nov 28	19.8	17.7
26215	20 31 51.64	−40 37 19.64	2021 Nov 28	9.9	8.4
24506	20 31 51.64	−40 37 19.64	2021 Nov 30	24.7	22.7
23843	20 31 51.64	−40 37 19.64	2022 Jul 26	19.8	17.8
26479	20 31 51.64	−40 37 19.64	2022 Jul 29	23.3	20.4

for a total of 256 ks spread over 10 observations (PI: S. A. Walker). All observations were done with the ACIS-S. The obsID, dates of observation, approximate exposure times, and cleaned exposure times are listed in Table 1.

2.1. Data Reduction

All data reduction was performed using CIAO, Chandra's data analysis system (version 4.14; Fruscione et al. 2006) and CALDB, the calibration database (version 4.10.2) provided by the Chandra X-ray Center. The primary data set given by the detector is an events list file of photons with measurements like the spatial resolution of the X-ray photons that arrive at the detector, the time of arrival, and the energy of that photon, called event 1 files. These event 1 files were reprocessed using the `chandra_repro` script, taking into account the most recent calibrations to the detector, by applying the latest charge transfer inefficiency correction, time-dependent gain adjustment, and the gain map to obtain the appropriate response files, new bad pixel files, and the processed level 2 event files. The `deflare` routine, which uses the `lc_clean` script created by M. Markevitch, was used to detect and get rid of flares and periods of anomalously low count rates from the input light curves. As can be seen in Table 1, the data were mostly clean and the final cleaned exposure was 225 ks.

The cleaned and reprocessed files were reprojected to create a merged image using `merge_obs` in the soft band (0.5−2.5 keV) and in the broad band (0.7−7.0 keV) and a merged event file and exposure-corrected images were created. The `merge_obs` script combines the `reproject_obs` and `flux_obs` scripts. The `reproject_obs` script finds the appropriate ancillary response files (ARFs) for all the event 2 files, matches up with the observations, and creates a new single event file by merging the event files of individual observations. The `flux_obs` script creates exposure maps and an exposure-corrected image. The bright point sources in the exposure-corrected image were removed by first excluding regions by eye, and the excluded regions were filled in using the `dmfilth` script. This script replaces the pixel values in the excluded regions of the image with values interpolated from the surrounding regions using a Poisson probability distribution.

Blank-sky observations were extracted using the `blanksky` script, which were then reprojected to match the coordinates of the observation. The blank-sky backgrounds were normalized by matching their count rate in the 9.5−12 keV energy band to that of the observed data set, thus ensuring uniformity.

3. Image Analysis

Figure 1 shows an exposure-corrected image of the cluster created by combining all the individual Chandra observations, with the point sources removed in the 0.5−7.0 keV energy band. The geometry of the image suggests that the system recently underwent a merger where the subclusters passed through each other along the east–west direction. The X-ray emission is seen extended from the southeast to the northwest direction. Two sharp surface brightness edges can be seen here, the "Primary Shock" in the northwestern region and the "SE edge" in the southeastern region. The brightest X-ray peak lies behind the SE edge, and is marked by a blue cross in Figure 1. A secondary X-ray peak marked by a red cross in Figure 1 lies behind the Primary Shock in the northwest. In previous shallow 10 ks observations, only two bright peaks could be observed, and no edges were visible. These deep Chandra observations have helped to resolve the sharp brightness edges and also allow us to produce a more detailed temperature map.

In Figure 2, the Chandra X-ray contours from our new observations are superimposed on a Hubble Space Telescope (HST) image of SPT J2031. The grayscale image is the HST image of SPT J2031 obtained by using the F814W filter. The Chandra contours are overlaid on this optical image in green. The white dashed circles show the two brightest cluster galaxies (BCGs). BCG 1 is close to the primary X-ray peak, and BCG 2 is approximately at the location of the Primary Shock front and offset from the secondary X-ray peak. The direction of the merger axis is estimated to be roughly from the northwest to the southeast, passing through the center of the two galaxy distributions.

The BCG 2 shown in the figure is SMACSJ2031.8-4036, which has been extensively studied by deep HST and MUSE data as it is a strong lensing cluster. According to the mass modeling presented in Richard et al. (2015), the eastern component has mass $M_{\rm east} = 2.4 \times 10^{14}\, M_{\odot}$.

In galaxy cluster mergers, the galaxies within the subcluster behave like collisionless particles, and lead the baryonic gas after the collision. This lag between the motion of the subcluster galaxies and the baryonic gas can result in an offset between the centroids of the main mass distribution and the elongated peak in the X-ray emission (Canning et al. 2011). Comparing the contours representing the brightest X-ray peaks in Figure 1 with the BCGs in Figure 2, there is an offset of the brightest X-ray peaks from the BCGs, indicating that the system recently underwent a merger. In Figure 2, the brightest X-ray peak is offset from BCG 1 by $\sim 0\rlap{.}'12$ (∼36 kpc), and the

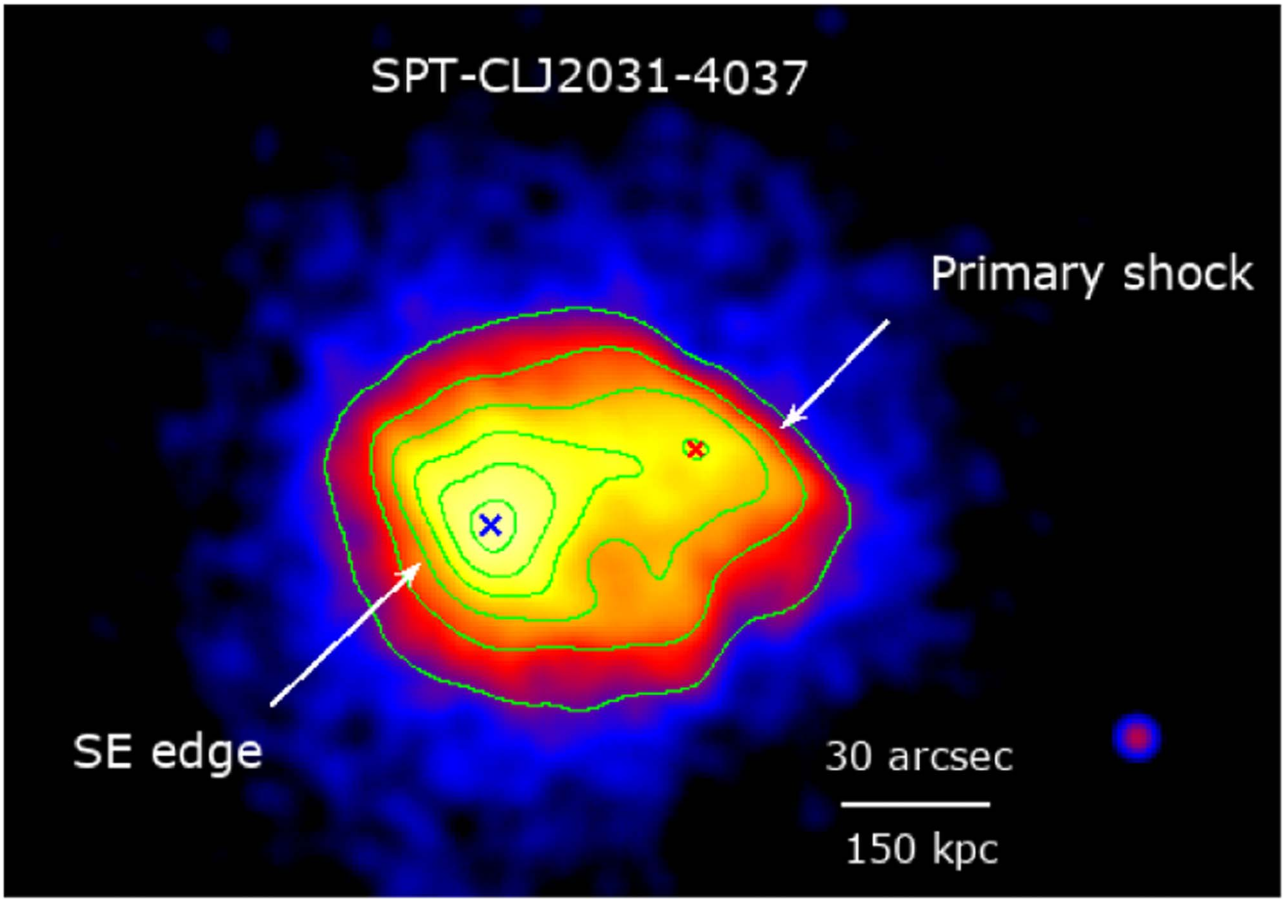

Figure 1. An exposure-corrected image of SPT J2031 with the point sources removed in the 0.5−7.0 keV energy range, smoothed with Gaussian $\sigma = 3$. North is up and east is to the left. Two sharp surface brightness edges are seen here, the Primary Shock in the northwest and the SE edge in the southeast of the image. The brightest X-ray peak lies behind the SE edge, marked by the blue cross. An additional X-ray peak lies behind the Primary Shock, marked by a red cross. The green lines represent Chandra contours.

secondary X-ray peak is offset from BCG 2 by $\sim 0\overset{'}{.}39$ ($\sim$117 kpc).

We obtained a GGM-filtered image of the merger, as shown in Figure 3 in the 0.5−7.0 keV energy range. GGM filtering is a robust edge-detection technique which is very useful in resolving the substructures in a cluster core, as well as at cluster outskirts. This filter calculates the gradient of an image assuming Gaussian derivatives, with the intensity of the GGM images indicating the slope of the local surface brightness gradient, where steeper gradients show up as brighter regions (Sanders et al. 2016). GGM images have been utilized in various scientific fields, including physics and astronomy, to map substructures with great visible clarity (Walker et al. 2016).

For the presented GGM image in Figure 3, we applied a 3 pixel scale filter, binning the Chandra image by a factor of 2 to yield pixels of width $0\overset{''}{.}949$. This GGM image reveals two surfaces with pronounced brightness gradients: the Primary Shock and SE edge, delineated by dashed red lines in Figure 3. In order to further investigate these edge features, we used spatial-spectroscopy techniques.

4. Spatially Resolved Spectroscopy

Spatially resolved spectroscopic techniques were used to produce maps of projected gas properties of the cluster (see Figure 4). The central $\sim 3' \times 3'$ region was divided into bins using the contour binning algorithm (Sanders 2006), which creates bins based on the variations in surface brightness. The signal-to-noise ratio (S/N) was chosen to be 32 ($\sim$1000 counts) for obtaining the bins, as was used in Russell et al. (2012). For all the 66 regions obtained this way, spectra were extracted for each observation and appropriate redistribution matrix files and ARFs were generated. The background for each of these spectra were subtracted using the normalized blank-sky backgrounds, as discussed in Section 2.1. These spectra were restricted to the energy range of 0.5–7.0 keV. The spectra for each region were then simultaneously fitted for all observations using Sherpa with the PHABS(APEC) model, where the hydrogen column density is fixed at $n_{\rm H} = 3.0 \times 10^{20}$ cm^{-2} (Kalberla et al. 2005), the solar abundance is 0.3 $Z_{\odot}$, and the redshift is 0.34, and C statistics were applied. The pseudopressure map is produced by multiplying the square root of the emission measure and temperature maps.

The panels in the top row and the bottom left of Figure 4 show the projected emission per unit area map (units of cm^{-5} arcsec^{-2}), projected temperature map (units of keV), and projected pseudopressure map (units of keV cm^{-5} arcsec^{-2}) from left to right, while the bottom right panel is the GGM image at a scale of 3 pixels.

Each edge in the GGM image corresponds to a jump in temperature in the temperature map and a jump in pressure in the pseudopressure map. This makes the edges consistent with being shock fronts.

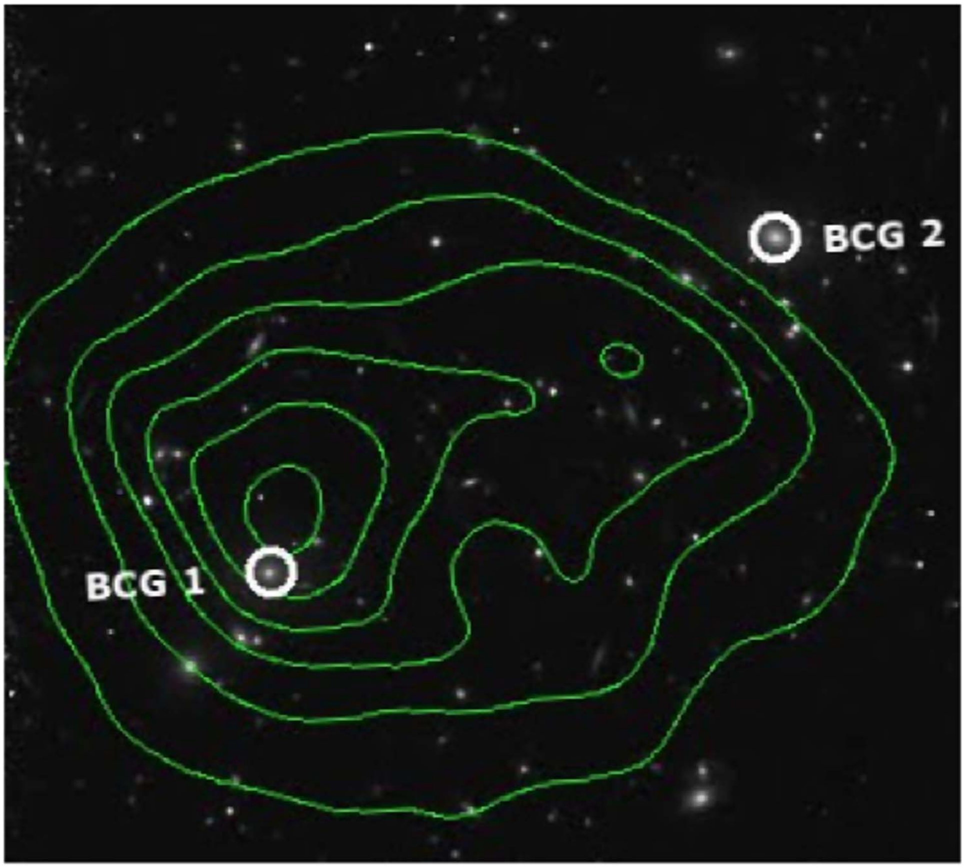

Figure 2. The grayscale image is an HST image of SPT J2031 obtained using the F814W filter. The white dashed circles show the two subclusters with their BCG. BCG 1 is close to the primary X-ray peak, and BCG 2 is approximately at the location of the Primary Shock front. The coordinates are shown to be accurate by a number of well-matched point sources.

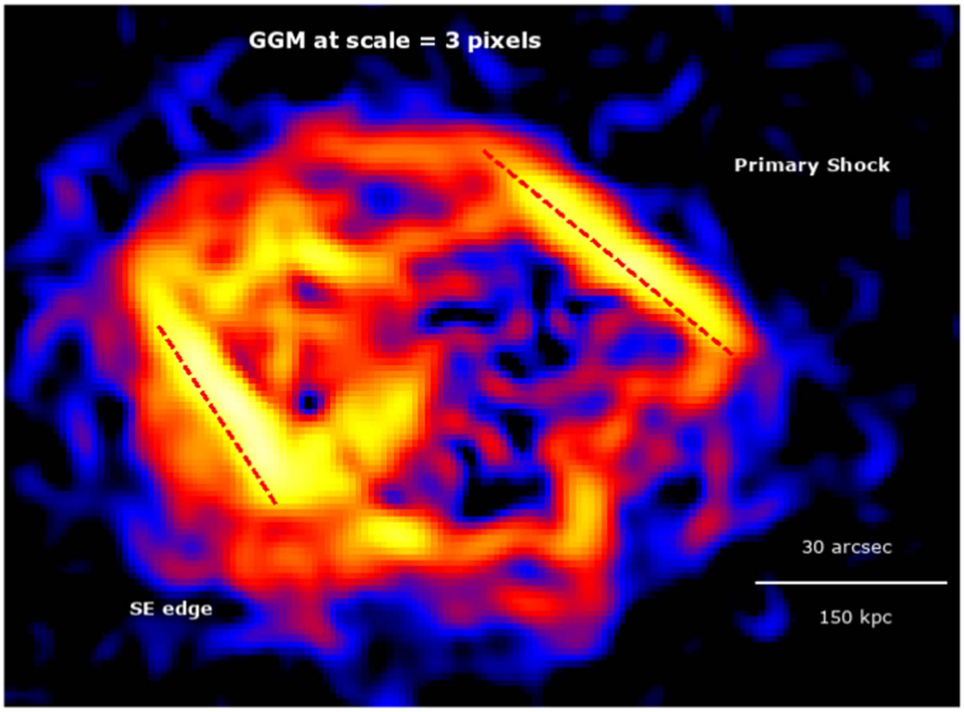

Figure 3. GGM image of SPT J2031 in the 0.5−7.0 keV energy range at scale = 3 pixels. The red dashed lines highlight the two surfaces with pronounced gradients, the Primary Shock in the northwest and the SE edge in the southeastern direction.

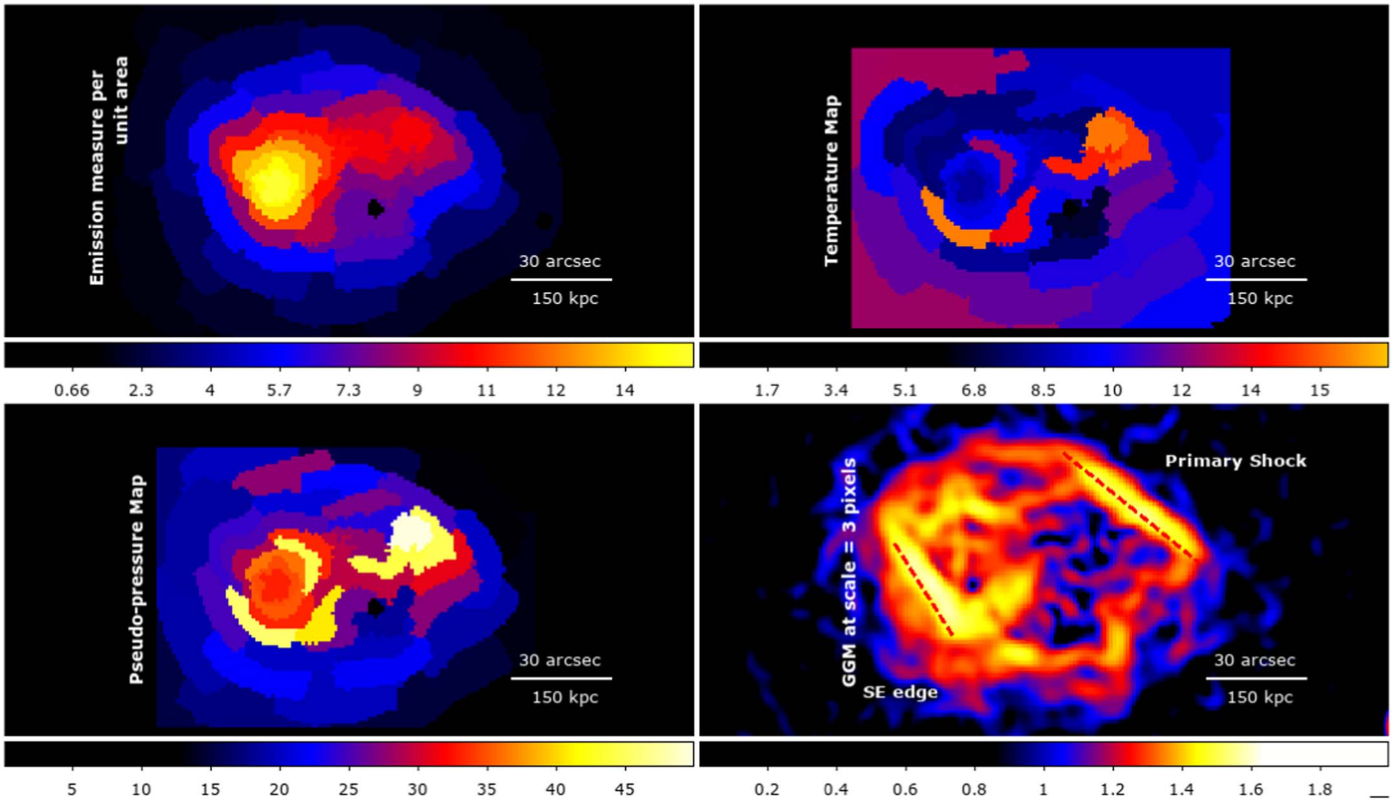

Figure 4. Top left: projected emission per unit area (units of cm^{-5} arcsec^{-2}). Top right: projected temperature map (keV) with S/N = 32. Bottom left: projected pseudopressure map (units of keV cm^{-5} arcsec^{-2}), obtained by multiplying the emission measure and temperature maps. The small black circles in the emission, temperature, and pseudopressure maps are the excluded point sources. Bottom right: GGM image of SPT J2031 in the 0.5−7.0 keV energy range at scale = 3 pixels.

5. Shock Fronts

While a number of clusters have been found to have shock-heated regions, the detection of a cluster merger with sharp surface brightness edges and a distinctive high-temperature jump is rare due to the requirement of favorable merger geometry (ZuHone & Su 2022). In fact, only a handful of merger shock fronts with a high Mach number, $M > 2.0$, have been discovered by Chandra, such as the Bullet Cluster with $M = 3.0 \pm 0.4$ (Markevitch 2006), A2146 with $M = 2.3 \pm 0.2$ (Russell et al. 2010, 2012, 2022), A665 with $M = 3.0 \pm 0.6$ (Dasadia et al. 2016), El Gordo with $M \geqslant 3$ (Botteon et al. 2016), A520 with $M = 2.4^{+0.4}_{-0.3}$ (Wang et al. 2018), and A98 with $M = 2.3 \pm 0.3$ (Sarkar et al. 2022). Chandra has also determined shock fronts with $M < 2.0$, such as for A2744 with $M = 1.41^{+0.13}_{-0.08}$ (Owers et al. 2011), A754 with $M = 1.57^{+0.16}_{-0.12}$ (Macario et al. 2011), A521 with $M = 2.4 \pm 0.2$ (Bourdin et al. 2013), and A2034 with $M = 1.59^{+0.06}_{-0.07}$ (Owers et al. 2014).

To determine the Mach number for SPT J2031, we extracted surface brightness profiles and temperature profiles across both the shock fronts.

5.1. Surface Brightness Profiles

Sharp discontinuities in the X-ray surface brightness are observed in Figure 1 and in the top left panel of Figure 4. In order to investigate these discontinuities, we extracted surface brightness profiles in the northwestern region covering the Primary Shock front and in the southeastern region covering the SE edge. Consistent with previous studies (Russell et al. 2010, 2012, 2022), our initial analysis assumed spherical geometry to derive these profiles. However, in subsequent analysis, we also explored an alternative approach by extracting the profiles using elliptical annuli as seen in Ogrean et al. (2014). This additional analysis aimed to ascertain whether an elliptical geometry provides a more accurate description of the shock geometry.

5.1.1. Spherical Geometry

The left panel of Figure 5 shows the sectors selected for extracting surface brightness profiles assuming a spherical geometry. The sectors are chosen to cover the region where the shock fronts are well defined, based on the GGM image. Sectors P1−P9 (where P refers to the Primary Shock) extend over the Primary Shock front. These sectors are centered so as to fully analyze the jump in surface brightness. The outer radius for each sector was taken to be $5'$ (although the sectors in the image extend only up to $\sim 1\overset{\prime}{.}5$). Taking into account that BCG 2 lies in the direction of these sectors, we excluded the region containing BCG 2 before extracting the surface brightness profiles. This was done to prevent any potential impact from BCG 2 on our analysis.

Once extracted, the surface brightness profiles were fitted with a broken power-law model projected along the line of sight (Markevitch & Vikhlinin 2007) with the aim to identify density discontinuities in the chosen sectors. Assuming spherical symmetry (following Russell et al. 2012), the density

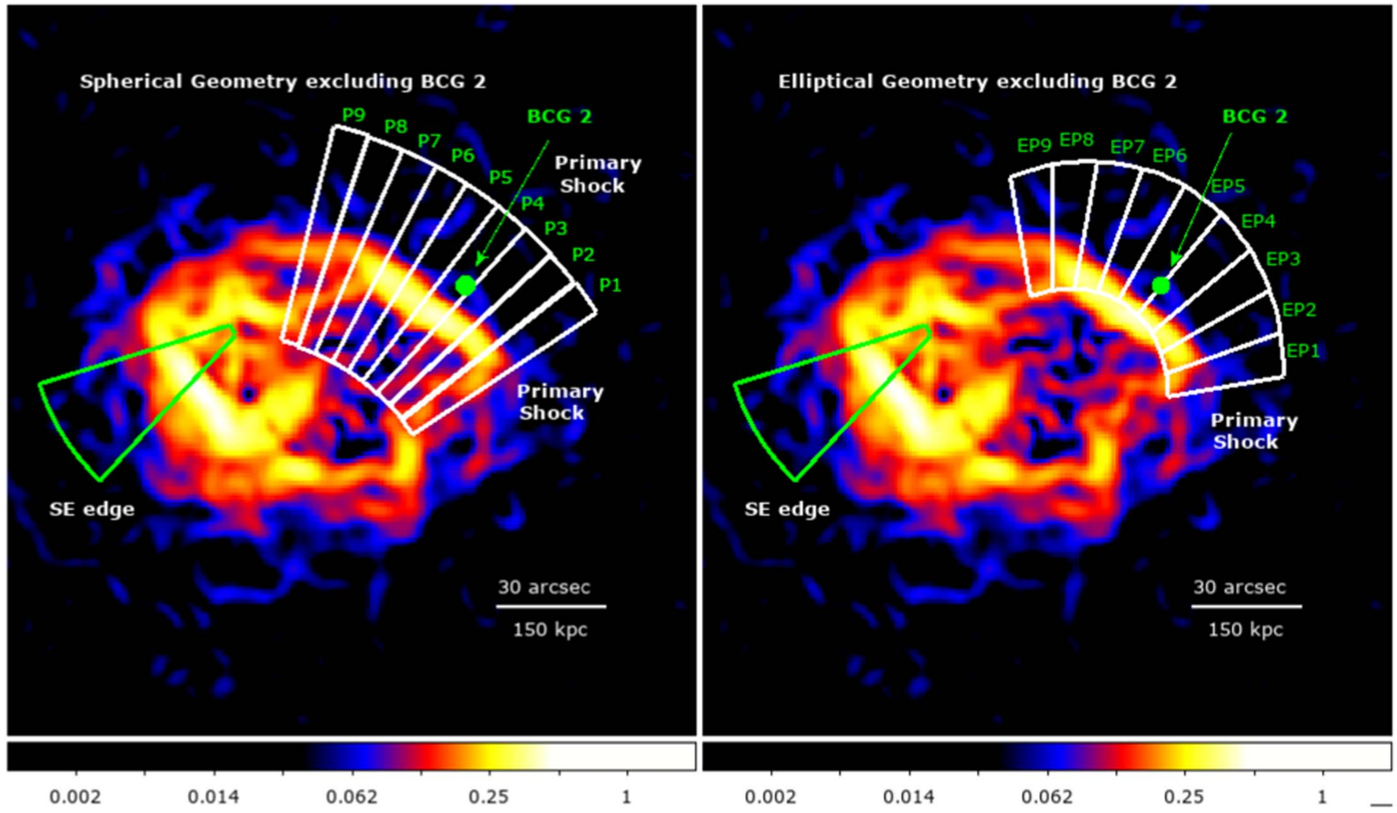

Figure 5. GGM image at scale = 3 pixels showing the sectors used to extract the surface brightness profiles assuming spherical geometry (left) and elliptical geometry (right). The sectors in white are used to measure the density jump across the Primary Shock and the one in green for the SE edge. The filled green circle is BCG 2, which is excluded while extracting the surface brightness profiles.

distribution can be given by

$$n(r) = \begin{cases} n_0\left(\dfrac{r}{r_{sh}}\right)^{\alpha_1}, & \text{if r } \leqslant \text{r}_{sh}, \\ \dfrac{1}{C}n_0\left(\dfrac{r}{r_{sh}}\right)^{\alpha_2}, & \text{if r } > \text{r}_{sh}, \end{cases} \tag{1}$$

where n_0 is the density normalization, α_1 and α_2 are power-law indices, and r_{sh} is the assumed shock location where the discontinuity in the surface brightness occurs. Also $C = \rho_2/\rho_1$, where ρ_2 is the postshock density and ρ_1 is the preshock density. At the location of the shock, ρ_2 is greater than ρ_1, (Mirakhor et al. 2023).

Using Rankine–Hugoniot jump conditions for the density jump, the Mach number for each sector can be calculated as follows:

$$M = \left[\frac{2\frac{\rho_2}{\rho_1}}{\gamma + 1 - (\frac{\rho_2}{\rho_1})(\gamma - 1)}\right]^{\frac{1}{2}}, \tag{2}$$

where ρ_2/ρ_1 is the density jump and $\gamma = 5/3$ for a monoatomic gas (Russell et al. 2010).

In Figure 6, the red crosses in each panel show the surface brightness profile across sectors P1–P9. For each of these sectors there is a sharp discontinuity in the surface brightness. The regions to the right of this jump are the preshock regions and the ones to the left, with the higher surface brightness, are the postshock regions.

We have binned sectors P1–P2, P3–P6, and P7–P9 so that the sectors containing the part of the edge with the highest density jump (P3–P6) are binned together. This binning allows us to better constrain the values of the density jumps, and how the density jump varies along the shock front. Sectors P3–P6 are designed to cover the steepest part of the jump based on the GGM image, while the regions P1–P2 and P7–P9 cover the regions to either side of the steepest jump. All three plots in Figure 7 show the surface brightness profiles over sectors P1–P2, P3–P6, and P7–P9 fitted with the broken power-law model, as indicated by the solid blue line. Table 2 shows the power-law indices and the density jump obtained from this fitting. The table shows these values for all the individual sectors P1–P9, the binned sectors P1–P2, P3–P6, and P7–P9, and the SE edge.

The density jump and Mach number obtained from sectors P1–P9 along the Primary Shock are plotted in Figure 8. The panel on the left shows the density jumps across the sectors plotted against the angle around the Primary Shock front going from 33° to 77°. The red crosses indicate the density jump across each individual sector P1–P9. The blue crosses represent the sectors binned as P1–P2, P3–P6, and P7–P9. The panel on the right shows the Mach numbers derived from the corresponding density jumps using Equation (2), also plotted against the angle around the Primary Shock front. The red crosses represent the Mach number derived for each of the sectors P1–P9 and blue crosses represent the binned sectors P1–P2, P3–P6, and P7–P9.

In both the plots, the observed trend is that the density jump and Mach number are highest at the center of the shock front where the GGM image shows the highest gradient. On both sides of this center point, as the brightness of the GGM image decreases, the values of the density jump and Mach number taper off, as expected from a similar analysis performed in

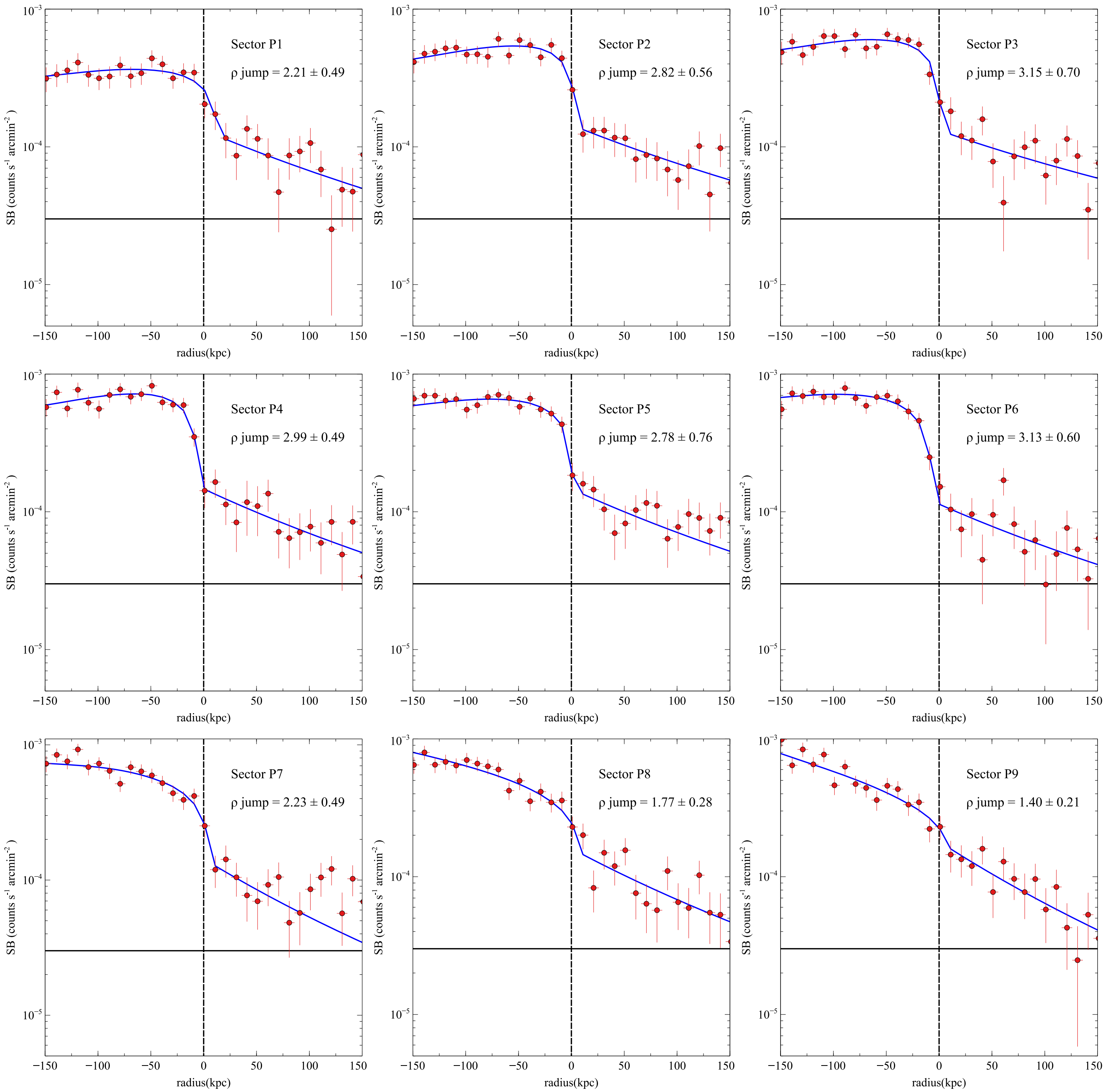

Figure 6. Surface brightness profiles in the 0.5−2.5 keV energy band across sectors P1–P9, where each is background subtracted (solid black) and fitted with a broken power-law density model (in blue).

Russell et al. (2022). The peak values of the density jump and Mach number are 3.11 ± 0.32 and $3.23^{+0.89}_{-0.56}$, respectively, for the binned sector P3–P6, the brightest region in the GGM image.

5.1.2. Elliptical Geometry

The surface brightness profiles can also be extracted by assuming elliptical geometry to better describe the geometry of the shock, following Ogrean et al. (2014). The ellipse chosen for this purpose has a major axis of 5′, a minor axis of 3.01′, and an angle between the major axis and the R.A. axis of 330°. The right panel of Figure 5 shows the sectors (EP1–EP9) used to extract the surface brightness profiles, where the white sectors represent the Primary Shock front, the green sector represents the SE edge, and the circle filled in green is the region where BCG 2 lies, and was hence excluded before extracting the profiles.

As described previously, once the surface brightness profiles are extracted, they are fitted with the broken power-law model to obtain the density profiles. Figure 9 shows the surface brightness (in red) across each of these sectors. After subtracting the background (in solid black), these profiles are fitted with the broken power-law density model (in blue). Furthermore, the sectors are binned as EP1–EP2, EP3–EP6,

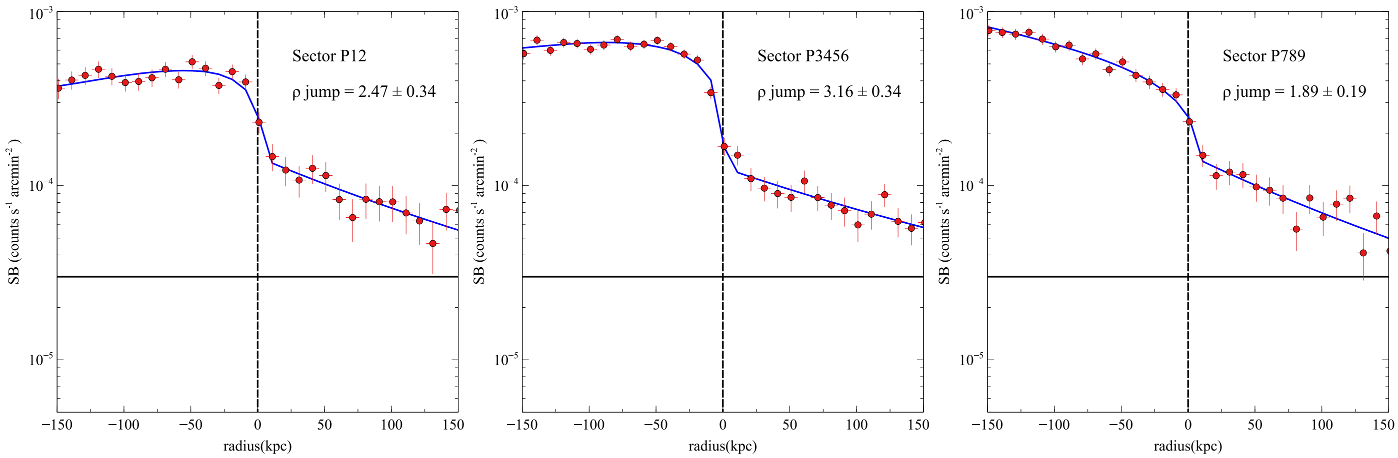

Figure 7. Surface brightness profiles across sectors P1–P2 (left panel), P3–P6 (center panel), and P7–P9 (right panel) in the 0.5−2.5 keV energy band. Each profile has been background subtracted and fitted with a broken power-law density model (in blue).

Table 2
Details of the Surface Brightness Fitting across the Sectors along the Primary Shock Front

Sector	Density Jump	M	α_1	α_2	χ^2/ν
P1	2.21 ± 0.55	$1.92^{+0.43}_{-0.29}$	−1.80 ± 0.83	2.17 ± 0.63	19.62/25
P2	2.8 ± 0.52	$2.65^{+1.39}_{-0.83}$	−2.67 ± 0.65	2.08 ± 0.50	14.11/25
P3	3.15 ± 0.7	$3.35^{+1.95}_{-0.85}$	−2.33 ± 0.48	1.87 ± 0.55	27.49/25
P4	2.99 ± 0.49	$2.99^{+1.03}_{-0.52}$	−2.55 ± 0.55	2.33 ± 0.47	17.65/25
P5	2.78 ± 0.77	$2.63^{+1.41}_{-0.62}$	−1.89 ± 0.29	2.30 ± 1.01	13.98/25
P6	3.13 ± 0.6	$3.3^{+1.91}_{-0.73}$	−1.55 ± 0.44	2.23 ± 0.55	20.43/25
P7	2.23 ± 0.49	$1.94^{+0.43}_{-0.28}$	−4.85 ± 0.2	2.94 ± 1.01	23.14/25
P8	1.77 ± 0.29	$1.54^{+0.18}_{-0.14}$	0.53 ± 0.38	2.60 ± 0.53	23.32/25
P9	1.4 ± 0.21	$1.27^{+0.12}_{-0.09}$	0.95 ± 0.39	3.04 ± 0.52	23.28/25
$P1-2$	2.47 ± 0.34	$2.2^{+0.35}_{-0.23}$	−2.56 ± 0.51	2.16 ± 0.37	17.37/25
$P3-6$	3.16 ± 0.34	$3.36^{+0.87}_{-0.48}$	−1.63 ± 0.19	1.86 ± 0.27	23.28/25
$P7-9$	1.89 ± 0.19	$1.64^{+0.12}_{-0.09}$	0.53 ± 0.23	2.40 ± 0.30	16.86/25
SE edge	1.53 ± 0.14	$1.36^{+0.09}_{-0.08}$	−1.17 ± 0.43	1.45 ± 0.39	67.13/64

Note. The columns are, from left to right: sector label, density jump across that sector obtained by fitting with the broken power-law density model, Mach number obtained from the density jump, the inner and outer slopes (power-law indices in the broken power-law model), and the reduced χ^2 of the fit.

and EP7–EP9 so that the sectors with the maximum gradient in intensity in the GGM as well as the highest density jumps are binned together. The surface brightness profiles across these binned sectors are seen in Figure 10. We see that the highest density jump is observed in the binned sector EP3–EP6, with $\rho = 3.04 \pm 0.36$, corresponding to a Mach number of $M = 3.09^{+0.75}_{-0.43}$. The density jumps, Mach numbers, and the parameters used for the fitting for the individual and binned sectors, as well as the SE edge, can be seen in Table 3. The results for the individual and binned sectors for spherical and elliptical geometry for the individual and binned sectors are well in agreement with each other as seen in the comparison Table 4 in the Appendix.

The density jump and Mach number obtained from the elliptical sectors EP1–EP9 along the Primary Shock are plotted in Figure 11. The panel on the left shows the density jumps across the sectors plotted against the angle around the Primary Shock front going from 45° to 125°. The red crosses indicate the density jump across each individual sector P1–P9. The blue crosses represent the sectors binned as P1–P2, P3–P6, and P7–P9. The panel on the right shows the Mach numbers derived from the corresponding density jumps using Equation (2), also plotted against the angle around the Primary Shock front. The red crosses represent the Mach number derived for each of the sectors P1–P9 and blue crosses represent the elliptical binned sectors EP1–EP2, EP3–EP6, and EP7–EP9.

Similar to Figure 8, in both the plots, the observed trend is that the density jump and Mach number is highest at the center of the shock front where the GGM image shows the highest gradient. On both sides of this center point, as the brightness of the GGM image decreases, the values of density jump and Mach number taper off. The peak values of the density jump

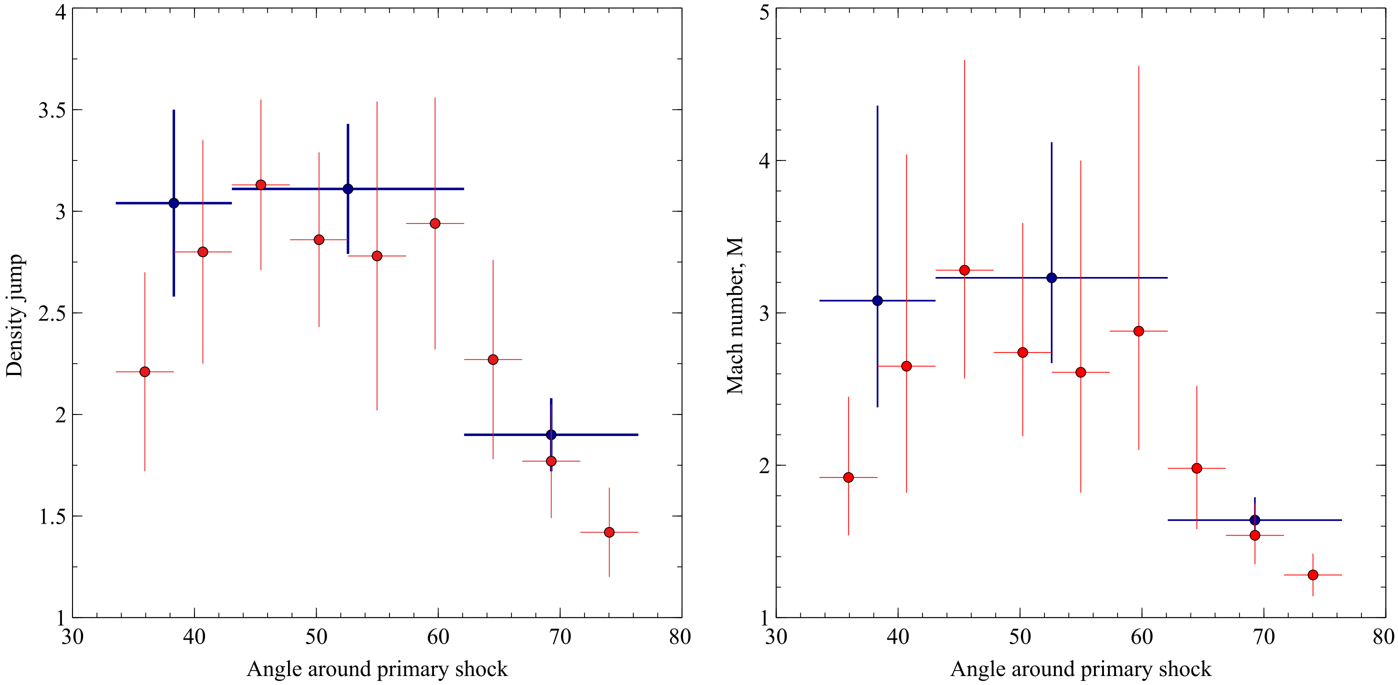

Figure 8. Left: the crosses and error bars in red depict the density jump (spherical geometry) across each of the sectors P1–P9 and the ones in blue represent the density jumps in sectors P1–P2, P3–P6, and P7–P9 from left to right. The *x*-axis represents the angle of the sectors around the Primary Shock front, going from 33° to 77°. Right: the Mach number, determined from the density jump, is shown here in red for the sectors P1–P9 and those for sectors P1–P2, P3–P6, and P7–P9 are shown in blue, across the angles of the sectors around the Primary Shock front.

and Mach number are 3.04 ± 0.36 and $3.09^{+0.75}_{-0.43}$, respectively, for the binned sector EP3–EP6, the brightest region in the GGM image.

Based on the values of the Mach number for the sectors P3–P6 and EP3–EP6 the Primary Shock in SPT J2031 is one of the strongest shocks, when compared with the Bullet Cluster with $M = 3.0 \pm 0.4$ (Markevitch 2006), A2146 with $M = 2.3 \pm 0.2$ (Russell et al. 2010, 2012, 2022), A665 with $M = 3.0 \pm 0.6$ (Dasadia et al. 2016), A520 with $M = 2.4^{+0.4}_{-0.3}$ (Wang et al. 2018), and A98 with $M = 2.3 \pm 0.3$ (Sarkar et al. 2022).

5.1.3. SE Edge

Figure 12 shows the surface brightness profile across the SE edge. The density jump across this edge is 1.53 ± 0.14, which corresponds to a Mach number of $1.36^{+0.09}_{-0.08}$. An analysis of the trend in the density jump and Mach number was not possible for the SE edge, as that edge is not spatially extended enough, and it does not have a high enough density jump or corresponding Mach number.

5.2. Spectral Analysis of the Shock Fronts

The changes in temperature and density across the surface brightness edges can be observed more accurately by extracting radial profiles over the sectors shown in Figure 13. The regions were selected so as to obtain the gas properties on both sides of each shock front. For the Primary Shock front, which has the higher density jump of the two, we extracted the temperature profile from the section of the shock with the highest density jump as determined in Section 5.1 corresponding to the sector P3–P6. Using `specextract` in Sherpa, spectra were extracted from each of the regions for each of the 10 observations. These spectra were then analyzed in the energy range of 0.5−7.0 keV. The background spectra used here were from the blank-sky backgrounds. The spectra for each region were then simultaneously fitted for all observations using Sherpa with the multiplicative PHABS(APEC) model, where the hydrogen column density is fixed at $n_{\rm H} = 3.0 \times 10^{20}$ cm^{-2} (Kalberla et al. 2005), the solar abundance is 0.3 $Z_{\odot}$, and the redshift is 0.34, and chi-squared statistics were applied. The resulting projected temperature profile for the Primary Shock is shown in the left panel of Figure 14. We see a significant temperature jump from about $7.0^{+0.7}_{-0.6}$ keV to $13.8^{+2.3}_{-1.8}$ keV. The projected temperature profile for the SE edge is shown in the right panel of Figure 14. We see a temperature jump from $6.48^{+0.63}_{-0.57}$ keV to $22.39^{+13.92}_{-9.02}$ keV. The gas in the preshock region of the Primary Shock has a temperature of $7.0^{+0.7}_{-0.6}$keV. Along with the sharp increase in the surface brightness, there is an observed increase in the temperature in the postshock region. The gas in this region has a temperature of $13.8^{+2.3}_{-1.8}$ keV. For the purpose of the fitting the abundance is fixed at 0.3 $Z_{\odot}$. We performed necessary checks to compare the temperature profiles across both the shock fronts with the temperature profile of the cluster along directions perpendicular to both shocks. Specifically, we extracted temperature profiles along the perpendicular directions of both shocks. Our analysis revealed no temperature jump in any of the directions perpendicular to both shocks. The left panel in Figure 15 shows the temperature profile across the Primary Shock front (in black) compared with the temperature profiles at +90° (in blue) and at −90° (in green). Similarly, the plot on the right compares the temperature profile of the SE edge (in black) with the temperature profiles at +90° (in blue) and at −90° (in green) from the SE edge. In both cases, it can be seen that the temperature profiles remain mostly flat in regions that are not associated with either shock front.

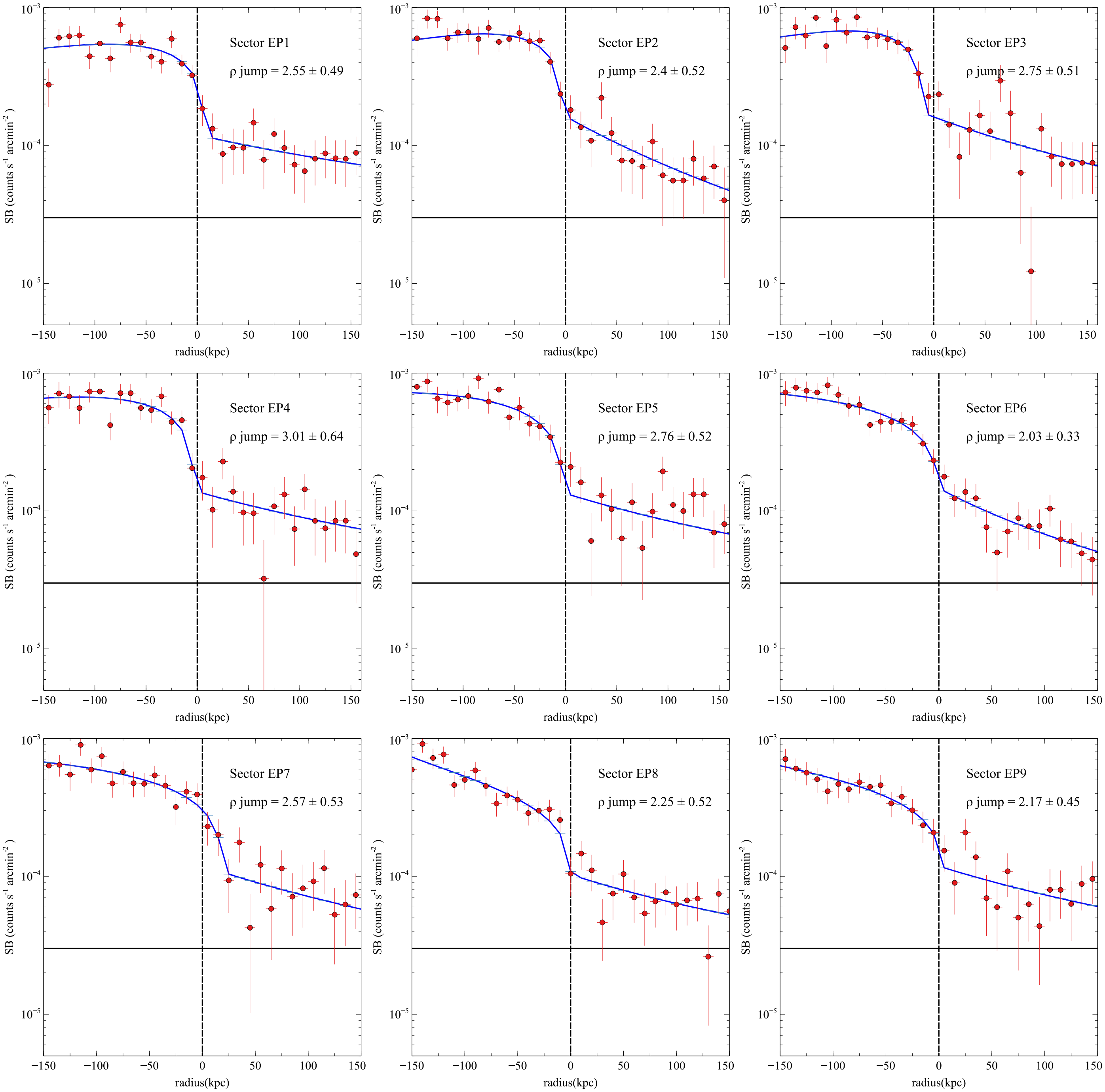

Figure 9. Surface brightness profiles (in red) in the 0.5−2.5 keV energy band across individual elliptical sectors EP1–EP9, fitted with the broken power-law density model (in blue) after performing background subtraction (solid black).

Following Russell et al. (2012), we also obtained the values of the deprojected electron temperature using PROJCT in XSPEC. PROJCT is a deprojection routine that assumes spherical geometry for the cluster. This seems to be a reasonable assumption because the shocks in SPT J2031 appear to be approximately circular in the plane of the sky. The preshock electron temperature is $7.0^{+0.7}_{-0.6}$ keV and the postshock deprojected electron temperature is $17.3^{+5.41}_{-3.48}$ keV. This allows us to calculate the Mach number using the deprojected temperature jump. The values for the deprojected temperature are plotted in the left panel of Figure 14 (red crosses).

We use the following Rankine–Hugoniot equation for the Mach number using the deprojected temperature jump:

$$M = \left[\frac{(\gamma+1)^2((\frac{T_2}{T_1})-1)}{2\gamma(\gamma-1)}\right]^{\frac{1}{2}}, \qquad (3)$$

where T_2/T_1 is the deprojected temperature jump. The Mach number from the temperature jump using the values obtained from the deprojected electron temperature after using this equation is $2.13^{+0.4}_{-0.38}$. The Mach number obtained using the temperature jump is lower than that obtained from the

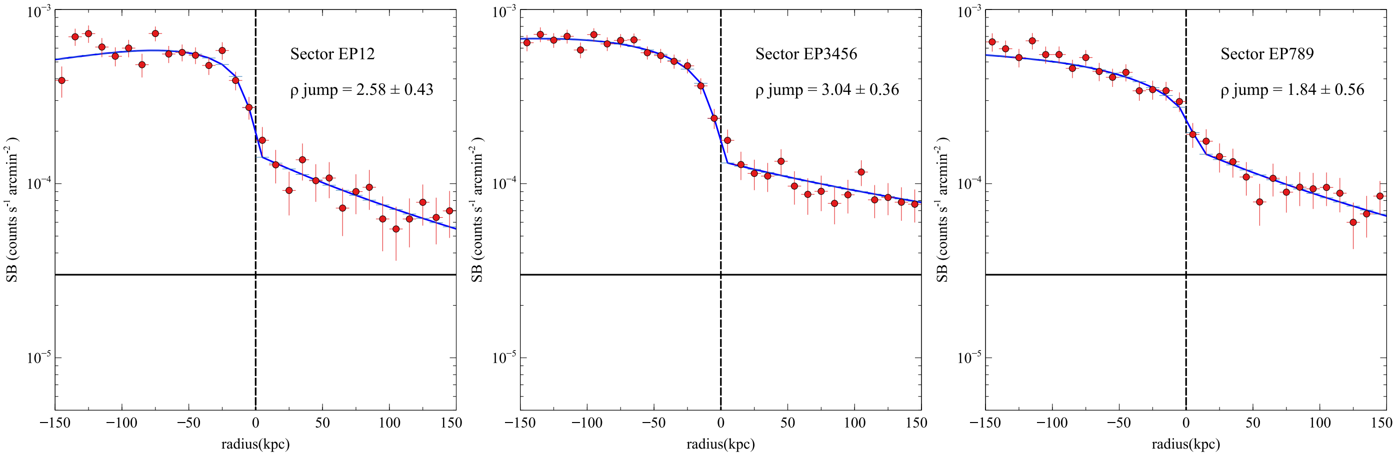

Figure 10. Surface brightness profiles across the sectors with elliptical geometry EP1–EP2 (left panel), EP3–EP6 (center panel), and EP7–EP9 (right panel) in the 0.5 −2.5 keV energy band. Each profile has been background subtracted and fitted with a broken power-law density model (in blue).

Table 3
Details of the Surface Brightness Fitting across the Sectors along the Primary Shock Front

Sector	Density Jump	M	α_1	α_2	χ^2/ν
EP1	2.55 ± 0.48	$2.3^{+0.57}_{-0.35}$	−0.96 ± 0.6	1.55 ± 0.3	24.39/25
EP2	2.4 ± 0.42	$2.12^{+0.41}_{-0.27}$	−1.12 ± 0.51	1.95 ± 0.44	8.4/22
EP3	2.75 ± 0.51	$2.58^{+0.76}_{-0.43}$	−1.17 ± 0.34	1.45 ± 0.24	42.2/40
EP4	3.01 ± 0.64	$3.03^{+1.62}_{-0.67}$	−0.64 ± 0.36	1.23 ± 0.24	38.2/40
EP5	2.76 ± 0.52	$2.59^{+0.79}_{-0.44}$	−0.26 ± 0.17	1.29 ± 0.22	41.85/46
EP6	2.03 ± 0.33	$1.76^{+0.24}_{-0.18}$	−0.06 ± 0.09	1.45 ± 0.2	27.50/31
EP7	2.57 ± 0.53	$2.32^{+0.64}_{-0.38}$	0.05 ± 0.17	1.39 ± 0.29	34.53/43
EP8	2.25 ± 0.52	$1.96^{+0.47}_{-0.31}$	0.46 ± 0.12	1.16 ± 0.25	28.03/231
EP9	2.17 ± 0.45	$1.89^{+0.37}_{-0.25}$	0.34 ± 0.17	1.33 ± 0.28	37.26/40
EP1−2	2.58 ± 0.43	$2.34^{+0.5}_{-0.32}$	−1.19 ± 0.63	1.72 ± 0.31	15.61/19
EP3−6	3.04 ± 0.36	$3.09^{+0.75}_{-0.43}$	−0.47 ± 0.11	1.17 ± 0.13	25.76/40
EP7−9	1.84 ± 0.56	$1.6^{+0.39}_{-0.27}$	−0.1 ± 0.99	1.65 ± 0.30	9.81/19
SE edge	1.29 ± 0.12	$1.19^{+0.06}_{-0.05}$	−0.9 ± 0.26	2.47 ± 0.15	27.04/25

Note. The columns are, from left to right: sector label, density jump across that sector obtained by fitting with the broken power-law density model, Mach number obtained from the density jump, the inner and outer slopes (power-law indices in the broken power-law model), and the reduced χ^2 of the fit.

density jump, which is similar to what is observed in Russell et al. (2012).

5.3. Electron–Ion Equilibrium

The observation of shock fronts in cluster mergers provides valuable insights into the process of electron–ion equilibration within the ICM. Cluster merger shock fronts affect electrons and ions differently. As the shock front passes through the ICM, it heats the ions in the ICM gas immediately owing to their smaller thermal velocities and greater mass compared to the electrons (ZuHone & Su 2022). This leads to a significant increase in ion temperature, not immediately observed in the electron temperature, which eventually equilibrates with the ion temperature. However, the mechanism of this shock heating remains debated (Wang et al. 2018). Presently the two models that can explain how the ICM gas is shock heated are the adiabatic-collisional model and the instant shock-heating model.

The adiabatic-collisional model posits that protons and heavier ions experience dissipative heating, while electrons undergo adiabatic compression to a temperature much lower than that of ions. This scenario arises due to the differing velocities of electrons and ions relative to the shock front. The ions move at a velocity slower than the shock, whereas the electrons, with a much lower mass compared to the ions, move at a much higher thermal velocity than the shock and thus are adiabatically compressed (Markevitch & Vikhlinin 2007). The temperature of

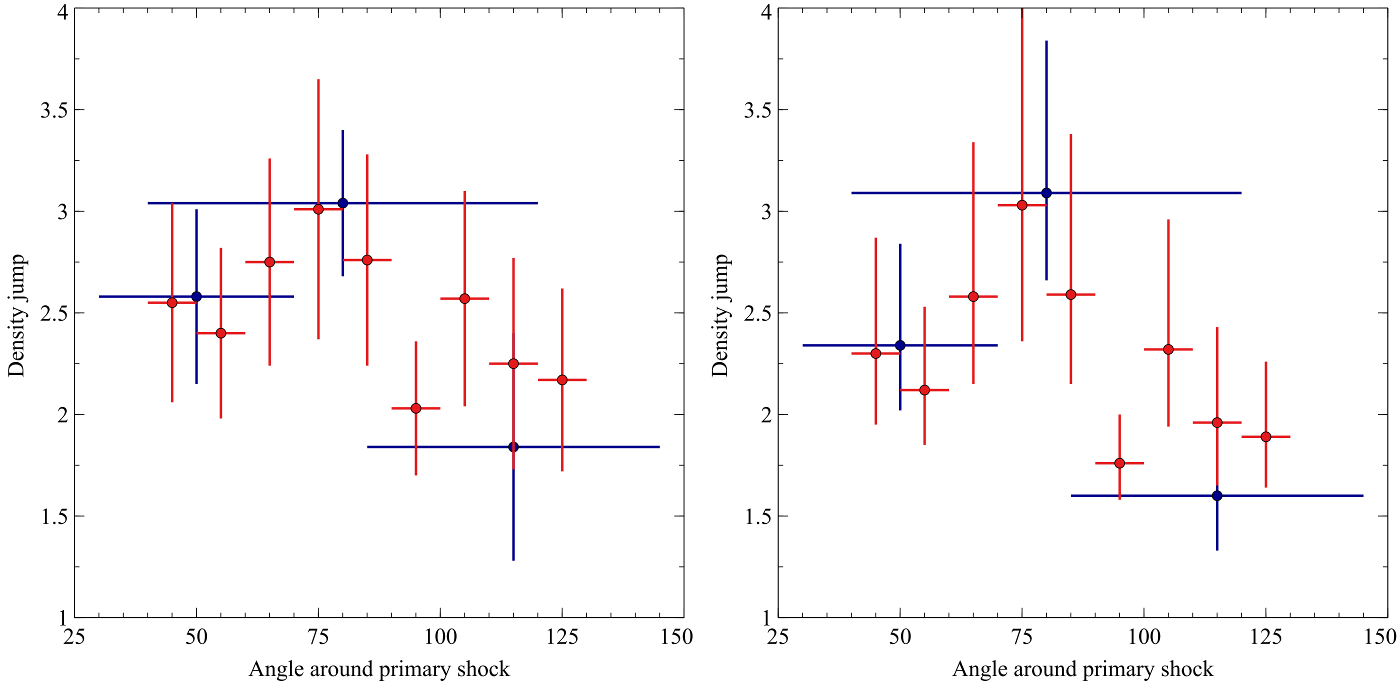

Figure 11. Left: the crosses and error bars in red depict the density jump (elliptical geometry) across each of the sectors EP1–EP9 and the ones in blue represent the density jumps in sectors EP1–EP2, EP3–EP6, and EP7–EP9 from left to right. The x-axis represents the angle of the sectors around the Primary Shock front, going from 45° to 120°. Right: the Mach number, determined from the density jump, is shown here in red for the sectors P1–P9 and those for sectors P1–P2, P3–P6, and P7–P9 are shown in blue, across the angles of the sectors around the Primary Shock front.

these adiabatically compressed electrons is given by

$$T_{e,2} = T_{e,1}\left(\frac{\rho_2}{\rho_1}\right)^{\gamma-1}, \tag{4}$$

where T_{e2} is the adiabatically compressed electron temperature, T_{e1} is the preshock electron temperature, $\left(\frac{\rho_2}{\rho_1}\right)$ is the density jump, where ρ_1 and ρ_2 are the preshock and postshock densities, respectively, and γ is the ratio of specific heats for a monoatomic gas. The electrons eventually undergo Coulomb collisions and attain thermal equilibrium with the ions over a timescale (Sarazin 1986) given by

$$\tau_{eq}(e, p) = 6.2 \times 10^8 yr\left(\frac{n_e}{10^{-3}}\right)^{-1}\left(\frac{T_e}{10^8 K}\right)^{3/2}, \tag{5}$$

where n_e is the electron density and T_e is the electron temperature.

The instant shock-heating model assumes that the ICM is a magnetized, collisionless plasma. This model has been proposed to explain observations of solar wind shocks, where electron and proton temperatures exhibit a jump on a linear scale of order several proton gyroradii, much smaller than their collisional mean free path (Markevitch & Vikhlinin 2007). The coupling of particles with electric and magnetic fields results in interactions with dissipation of scale much shorter than the collision mean free path (Russell et al. 2012). Hence, it is possible to find an electron–ion equilibration timescale shorter than the Coulomb timescale.

Following the conservation of the total kinetic energy density and assuming that the relation between the electron density (n_e) and ion density (n_i) is given by $n_e = 1.21 n_i$, the mean temperature of the gas ($T_{\rm gas}$) remains constant with time and is given by (ZuHone & Su 2022)

$$T_{gas} = \frac{(n_i T_i + n_e T_e)}{(n_i + n_e)} = \frac{T_i + 1.21 T_e}{2.21}. \tag{6}$$

The rate at which the electron and ion temperatures equilibrate via Coulomb collisions is given by

$$\frac{dT_e}{dt} = \frac{T_i - T_e}{t_{eq}}. \tag{7}$$

Rearranging this equation gives

$$\frac{t_{eq}}{T_i - T_e} dT_e = dT. \tag{8}$$

Integrating Equation (8) one can obtain the model electron temperature analytically (see Ettori & Fabian 1998). The emissivity-weighted electron temperature profile is projected along the line of sight by

$$\langle T \rangle = \int_{b^2}^{\infty} \frac{\epsilon(r) T_e(r) dr^2}{\sqrt{r^2 - b^2}} \int_{b^2}^{\infty} \frac{\epsilon(r) dr^2}{\sqrt{r^2 - b^2}}, \tag{9}$$

where $\epsilon(r)$ is the emissivity at radius r and b is the distance from the shock front (Sarkar et al. 2022).

Although we cannot measure the temperature of the ions, it is possible to measure the jump in the gas density across the shock front (which we have done in Section 5.1), which can be used to calculate the postshock equilibrium temperature for the electrons and ions using the Rankine–Hugoniot jump conditions from the preshock temperature (Landau & Lifshitz 1987). The temperature jump can be obtained using Equation (10) (Markevitch & Vikhlinin 2007):

$$\frac{T_2}{T_1} = \frac{\zeta - \rho_1/\rho_2}{\zeta - \rho_2/\rho_1}, \tag{10}$$

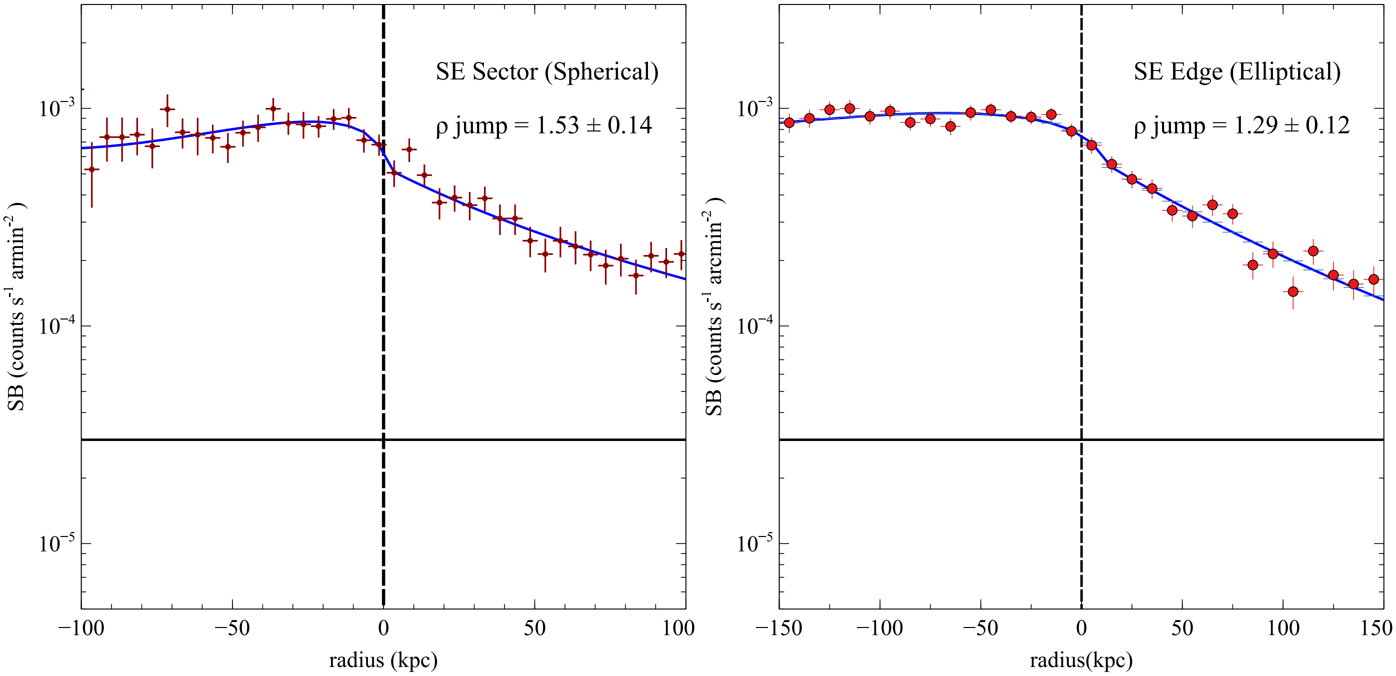

Figure 12. Surface brightness profile extracted in the 0.5−2.5 keV energy band over the SE edge using spherical (left) and elliptical (right) geometry. The profiles were background subtracted and fitted with a broken power-law density model (solid blue line) to obtain the density jump and Mach number. For the spherical geometry, the density jump obtained is 1.53 ± 0.14, which corresponds to a Mach number of $1.36^{+0.09}_{-0.08}$, whereas for the elliptical geometry, the density jump is 1.29 ± 0.12, corresponding to a Mach number of $1.19^{+0.06}_{-0.05}$. The dashed vertical line shows the shock location.

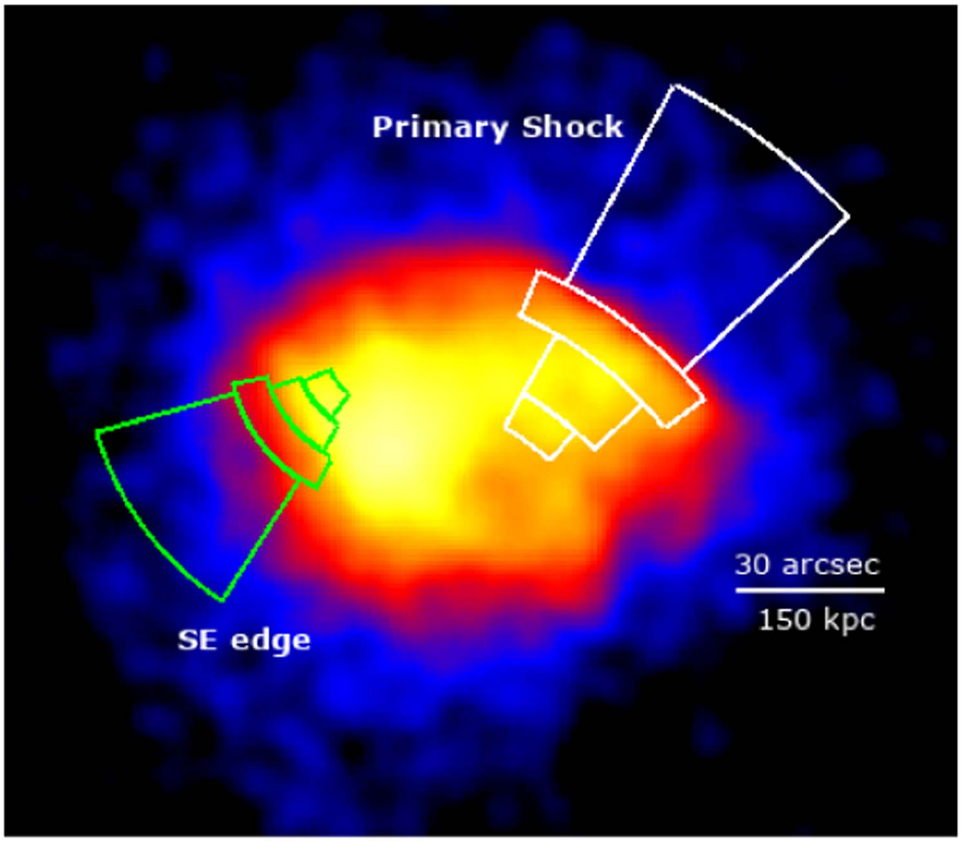

Figure 13. Exposure-corrected Chandra image of SPT J2031 in the 0.5–2.5 keV energy range with the regions that were used to extract the temperature profiles across both surface brightness edges.

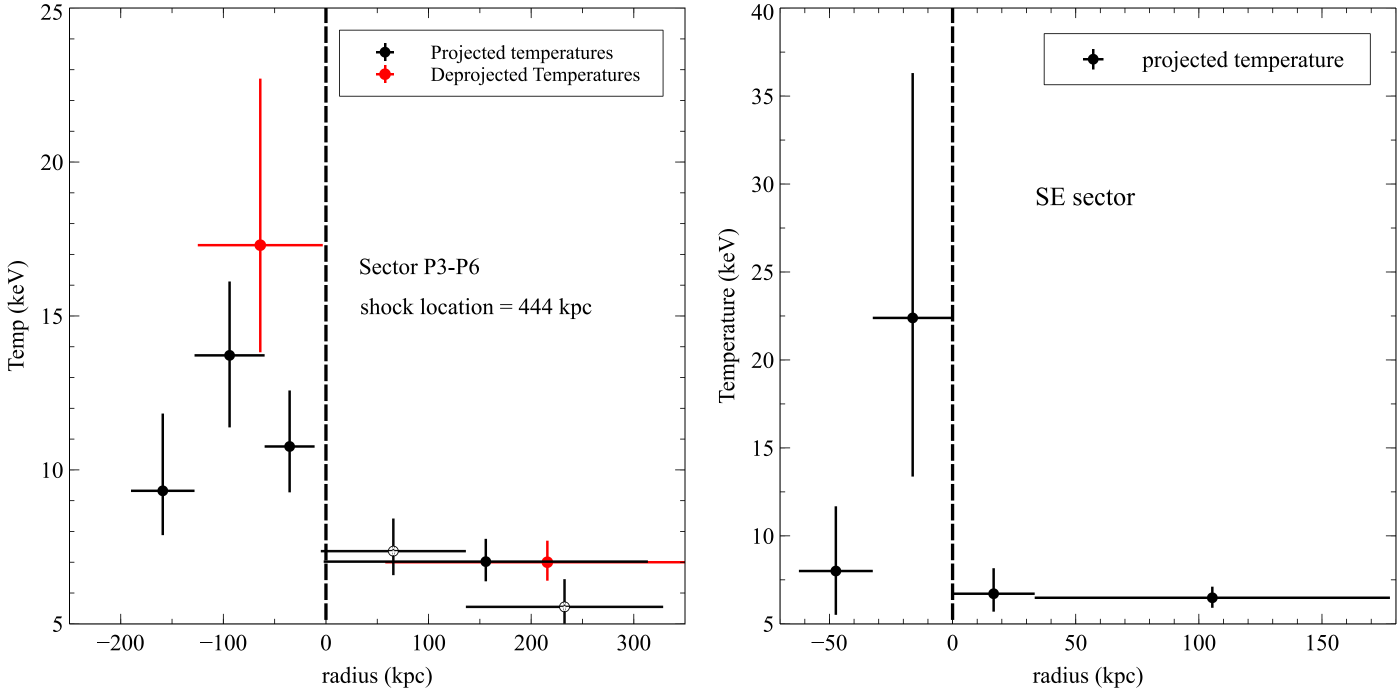

Figure 14. Left: the observed projected electron temperature profile (in black) over the Primary Shock front overlaid with the deprojected temperature profile (in red). The two data points with white circles in the preshock region represent narrower bins of width 150 kpc. We define the shock location to be at $r = 0$ kpc. Right: the figure shows the observed projected electron temperature profile across the SE edge. Again, we define the shock location to be at $r = 0$ kpc.

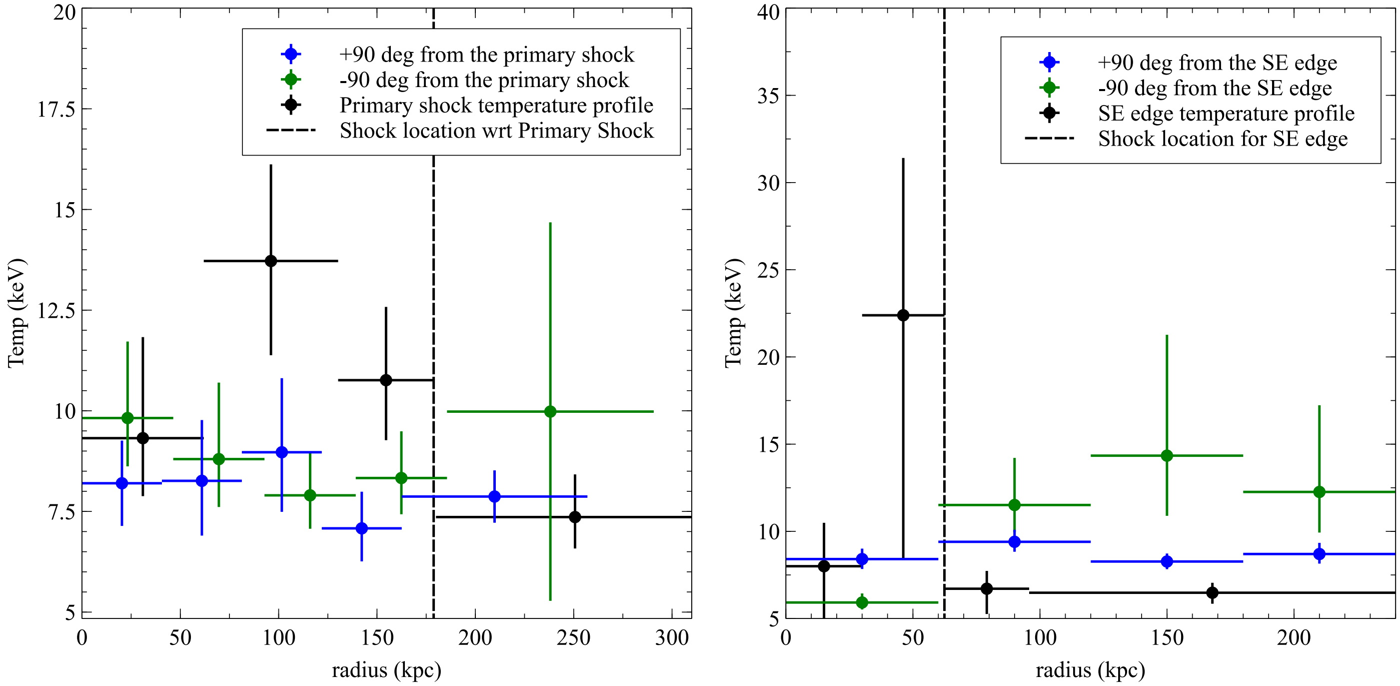

Figure 15. Left: comparison of the temperature profile across the Primary Shock (in black) with the temperature profiles at +90° (in blue) and at −90° (in green) from the Primary Shock front. Right: comparison of the temperature profile across the SE edge (in black) with the temperature profiles at +90° (in blue) and at −90° (in green) from the SE edge.

where we have assumed that $\gamma = 5/3$, the adiabatic index for monoatomic gas, and $\zeta \equiv (\gamma + 1)/(\gamma - 1)$, where the indices 1 and 2 denote the preshock and postshock quantities, respectively.

We did this for both the instant heating model and the collisional equilibration model as can be seen in Figure 16.

The bow shock in the Bullet Cluster provided the first ever opportunity to determine the timescale of electron–ion equilibration in a magnetized ICM (Markevitch 2006). The two models of heating were compared with the observed electron temperature profile. Markevitch (2006) shows tantalizing evidence supporting the instant equilibration model at 95% significance, as the postshock temperature in the cluster is very high (∼20−40 keV) and hence very difficult to constrain.

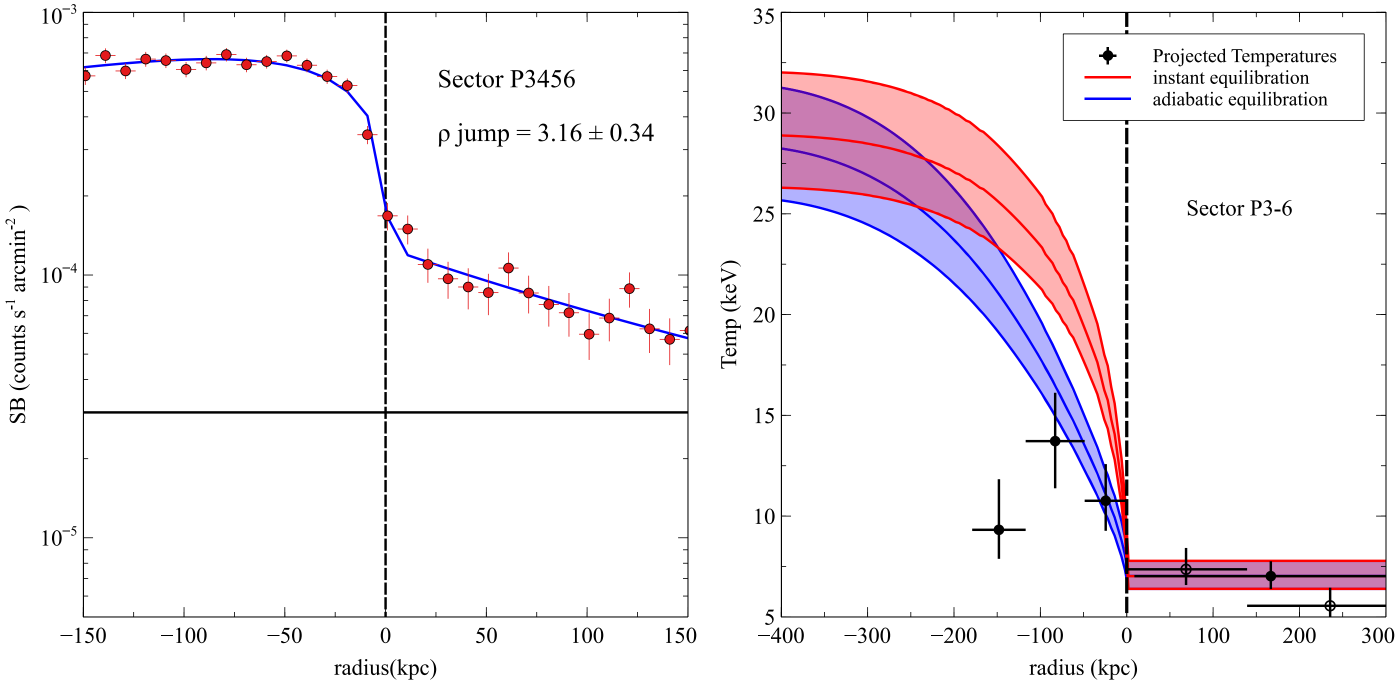

Figure 16. Left: surface brightness profiles extracted over sectors P3−P6 in the 0.5−2.5 keV energy band with BCG 2 excluded. The profiles are background subtracted and have been fitted with a broken power-law gas density model (in solid blue). The density jump observed over this sector is 3.16 ± 0.34 and the Mach number resulting from this density jump is $3.36^{+0.87}_{-0.48}$. Right: projected electron temperatures (in black) observed across the sectors P3−P6 of the Primary Shock front compared with the overlaid adiabatic-collisional (in blue) and instant heating models (in red) projected (up to 1σ error bands) along the line of sight for electron–ion equilibration. The preshock region shows the temperature value for a 300 kpc wide bin (in solid black) as well as two smaller bins of 150 kpc width (white-filled circles) each. The postshock temperature for the Primary Shock front seemingly favors the adiabatic-collisional model over the instant heating model.

The postshock temperatures for SPT 2031 are much lower than the Bullet Cluster (∼13−15 keV) and hence can be constrained much better. Additionally, the Mach number is sufficiently high to obtain the separation between the adiabatic and instant equilibration models.

The right hand panel of Figure 16 shows how the electron temperatures observed across the Primary Shock front compare with the collisional and instant heating models projected along the line of sight. The observed postshock temperature for the Primary Shock front seems to favor the collisional model over the instant heating model.

The models were generated by assuming spherical geometry. The cluster, which is assumed to be spherical, is divided into 1000 shells of uniform radii, and thereby have the same volume dV. The electron temperature along the line of sight was obtained for each shell and the corresponding emissivity is also obtained based on the density profile. The projected models were determined from the emissivity-weighted electron temperature. Using Equation (5). the electron–ion equilibration timescale for Coulomb collisions is calculated to be 0.2 Gyr.

In the case of the Bullet Cluster, Markevitch (2006) found that the observed temperature profile supports the instant equilibration model, suggesting that electrons at the shock front were heated on a timescale faster than the Coulomb collisional timescale. However, the postshock temperature in the Bullet Cluster is ∼20–40 keV, which is much higher than the energy passband of Chandra, thus making it difficult to constrain. The postshock electron temperature in SPT J2031 is lower than that of the Bullet Cluster, making the measurements of the postshock temperature more accurate. In contrast, an analysis of the shock in the Bullet Cluster with the Atacama Large Millimeter/submillimeter Array and the Atacama Compact Array (Di Mascolo et al. 2019) found that the assumption of an adiabatic temperature jump in the electron temperature results in the best agreement between results of Sunyaev–Zel'dovich and X-ray measurements.

For the merger shock front in A2146, Russell et al. (2012) found that the the temperature profile across the bow shock is consistent with the collisional equilibration model, whereas the upstream shock favors the instant equilibrational model. However the uncertainty in the measurement for the upstream shock was higher because of its lower Mach number and hence was not determined to be a definite conclusion. Subsequently, with deeper 2 Ms Chandra observations of A2146, Russell et al. (2022) found that both the shock fronts support the collisional equilibration model. Our results for the Primary Shock in SPT J2031 agree with Russell et al. (2012, 2022) in that the observed postshock electron temperature favors the collisional equilibration model.

An analysis of the merger shock front in A520 (Wang et al. 2018) found that the postshock electron temperature was higher than expected from a situation where the electrons undergo adiabatic compression followed by Coulomb collisions. Hence, like the Bullet Cluster, the electron temperature profile in A520 also supports the instant equilibration model with a confidence level of 95%.

A similar comparison of the postshock electron temperature in the merger shock of A98 (Sarkar et al. 2022) with the collisional and instant equilibrational model showed that the observed postshock electron temperature favors the instant equilibration model, however the large uncertainties in the temperature indicate that the collisional model cannot be ruled out.

The preshock sound speed, derived from the equations $c_s = \sqrt{\gamma k_B T / m_{\rm H} \mu}$ is $(1.3 \pm 0.06) \times 10^3$ km s^{-1}. The shock speed, obtained by multiplying the Mach number (from the density jump, $M = 3.23^{+0.89}_{-0.56}$) and the sound speed is $v_{\rm shock} \sim (4.4^{+0.27}_{-0.16}) \times 10^3$ km s^{-1}. The postshock velocity $v_{\rm ps}$ for the Primary Shock front is 1414 km s^{-1}, obtained by dividing the shock speed by the density jump.

6. Conclusions

We conducted a comprehensive analysis of our newly acquired deep (256 ks) Chandra observations of the merging system SPT J2031 and obtained the following results.

1. SPT J2031 exhibits merger geometry, as suggested by an offset between the brightest X-ray peaks in the exposure-corrected image from the Chandra observations and the two BCGs in the HST optical image.
2. We have utilized the GGM filtering technique to identify two sharp surface brightness edges in SPT J2031, the Primary Shock front and the SE edge.
3. We extracted surface brightness profiles (assuming spherical and elliptical geometries) across both the edges identified in the GGM image and fitted them with a broken power-law model to find the density jump across the shock front. The sharp edge in the northwest direction is the Primary Shock with density jump $\rho = 3.16 \pm 0.34$ corresponding to a Mach number of $3.36^{+0.87}_{-0.48}$ for spherical geometry and a density jump of $\rho = 3.04 \pm 0.36$ corresponding to a Mach number of $3.09^{+0.75}_{-0.43}$ for elliptical geometry.
4. Due to the high Mach number obtained from the density jump in the Primary Shock front, we were able to compare the observed electron temperature profile of the Primary Shock with the collisional equilibration model and the instant shock-heating model. We found that the postshock electron temperature is lower than the temperature predicted for the instant shock-heating model and favors the collisional equilibration model. These findings are similar to the result in Russell et al. (2012, 2022). However, we cannot completely rule out the instant heating model.
5. The other surface brightness edge, the SE edge, is observed in the southeastern direction and also appears to be a shock front. It has density jump $\rho = 1.53 \pm 0.14$, corresponding to Mach number $M = 1.36^{+0.09}_{-0.08}$ for spherical geometry and density jump $\rho = 1.29 \pm 0.12$, corresponding to Mach number $M = 1.19^{+0.06}_{-0.05}$. Since the Mach number $M < 2$, we were not able to achieve enough separation between the two projected models of heating to compare with the observed electron temperature profile.
6. We plotted the density jump and Mach number of the Primary Shock as a function of the angle around the shock front and found that the density jump, and subsequently the Mach number, peak at the center of the shock front, where the gradient in the GGM image is maximum. Both the density jump and the Mach number taper off with change in angle on both sides of this center point.

Acknowledgments

We gratefully acknowledge the valuable feedback provided by the referee, which enhanced the quality and clarity of this manuscript. We acknowledge support from Chandra grant GO1-22121X. We thank Florian Hofmann for helpful discussions. This work is based on observations obtained with the Chandra observatory, a NASA mission.

Software: CIAO (Fruscione et al. 2006), XSPEC (Arnaud 1996), and Proffit (Eckert et al. 2011).

Data Availability

This paper employs a list of Chandra data sets, obtained by the Chandra X-ray Observatory, contained in the Chandra Data Collection (CDC) doi:10.25574/cdc.229.

Appendix

As a part of our analysis, we had extracted surface brightness profiles assuming spherical geometry without excluding the region containing BCG 2 for completeness, and to check if BCG 2 indeed affected the brightness. Figures 5 and 17 compare the sectors used for this analysis with the sectors used for spherical and elliptical geometry where BCG 2 has been excluded. Table 4 compares the values of the density jumps and the corresponding Mach numbers obtained for all three cases. We find that for most regions, whether individual or binned, the results are well in agreement with each other.

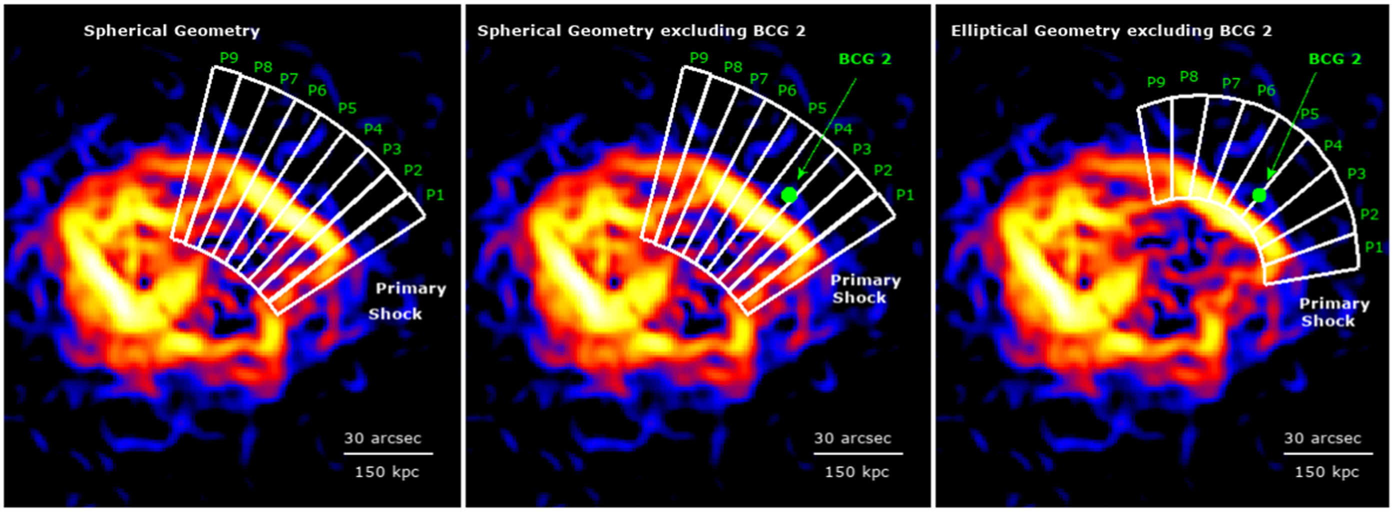

Figure 17. GGM image.

Table 4

Table of Comparison of Density Jumps and the Corresponding Mach Numbers

Spherical Geometry						Elliptical Geometry		
With BCG 2			Without BCG 2			Without BCG 2		
Sector	ρ	M	Sector	ρ	M	Sector	ρ	M
P1	2.21 ± 0.49	$1.92^{+0.53}_{-0.38}$	P1	2.21 ± 0.55	$1.92^{+0.43}_{-0.29}$	EP1	2.55 ± 0.49	$2.3^{+0.57}_{-0.35}$
P2	2.8 ± 0.55	$2.65^{+1.39}_{-0.83}$	P2	2.8 ± 0.52	$2.65^{+1.39}_{-0.83}$	EP2	2.4 ± 0.42	$2.12^{+0.41}_{-0.27}$
P3	3.13 ± 0.42	$3.28^{+1.38}_{-0.71}$	P3	3.15 ± 0.7	$3.35^{+1.95}_{-0.85}$	EP3	2.75 ± 0.51	$2.58^{+0.76}_{-0.43}$
P4	2.86 ± 0.43	$2.74^{+0.85}_{-0.55}$	P4	2.99 ± 0.49	$2.99^{+1.03}_{-0.52}$	EP4	3.01 ± 0.64	$3.03^{+1.62}_{-0.67}$
P5	2.78 ± 0.76	$2.61^{+1.39}_{-0.79}$	P5	2.78 ± 0.77	$2.63^{+1.41}_{-0.62}$	EP5	2.76 ± 0.52	$2.59^{+0.79}_{-0.44}$
P6	2.86 ± 0.57	$2.74^{+1.50}_{-0.73}$	P6	3.13 ± 0.6	$3.3^{+1.91}_{-0.73}$	EP6	2.03 ± 0.33	$1.76^{+0.24}_{-0.18}$
P7	2.27 ± 0.49	$1.98^{+0.54}_{-0.4}$	P7	2.23 ± 0.49	$1.94^{+0.43}_{-0.28}$	EP7	2.57 ± 0.53	$2.32^{+0.64}_{-0.38}$
P8	1.77 ± 0.28	$1.54^{+0.21}_{-0.19}$	P8	1.77 ± 0.29	$1.54^{+0.18}_{-0.14}$	EP8	2.25 ± 0.52	$1.96^{+0.47}_{-0.31}$
P9	1.42 ± 0.22	$1.28^{+0.14}_{-0.14}$	P9	1.4 ± 0.21	$1.27^{+0.12}_{-0.09}$	EP9	2.17 ± 0.45	$1.89^{+0.37}_{-0.25}$
P1−2	2.53 ± 0.42	$2.27^{+0.39}_{-0.31}$	P1−2	2.47 ± 0.34	$2.2^{+0.35}_{-0.23}$	EP1−2	2.58 ± 0.43	$2.34^{+0.5}_{-0.32}$
P3−6	3.11 ± 0.32	$3.23^{+0.89}_{-0.56}$	P3−6	3.16 ± 0.34	$3.36^{+0.87}_{-0.48}$	EP3−6	3.04 ± 0.36	$3.09^{+0.75}_{-0.43}$
P7−9	1.90 ± 0.18	$1.64^{+0.15}_{-0.13}$	P7−9	1.89 ± 0.19	$1.64^{+0.12}_{-0.09}$	EP7−9	1.84 ± 0.56	$1.6^{+0.39}_{-0.27}$

ORCID iDs

Purva Diwanji https://orcid.org/0000-0003-3621-2999
Stephen A. Walker https://orcid.org/0000-0002-6413-4142
M. S. Mirakhor https://orcid.org/0000-0002-7595-6723

References

Arnaud, K. A. 1996, in ASP Conf. Ser. 101, Astronomical Data Analysis Software and Systems V, ed. G. H. Jacoby & J. Barnes (San Francisco, CA: ASP), 17
Blandford, R., & Eichler, D. 1987, PhR, 154, 1
Böhringer, H., Schuecker, P., Guzzo, L., et al. 2004, A&A, 425, 367
Botteon, A., Gastaldello, F., Brunetti, G., & Kale, R. 2016, MNRAS, 463, 1534
Bourdin, H., Mazzotta, P., Markevitch, M., Giacintucci, S., & Brunetti, G. 2013, ApJ, 764, 82
Canning, R. E. A., Russell, H. R., Fabian, A. C., Crawford, C. S., & Hatch, N. A. 2011, MmSAI, 82, 662
Chiu, I., Mohr, J. J., McDonald, M., et al. 2018, MNRAS, 478, 3072
Dasadia, S., Sun, M., Sarazin, C., et al. 2016, ApJL, 820, L20
Di Mascolo, L., Mroczkowski, T., Churazov, E., et al. 2019, A&A, 628, A100
Eckert, D., Molendi, S., & Paltani, S. 2011, A&A, 526, A79
Ettori, S., & Fabian, A. C. 1998, MNRAS, 293, L33
Fruscione, A., McDowell, J. C., Allen, G. E., et al. 2006, Proc. SPIE, 6270, 62701V
Kalberla, P. M. W., Burton, W. B., Hartmann, D., et al. 2005, A&A, 440, 775
Landau, L. D., & Lifshitz, E. M. 1987, Fluid Mechanics (2nd ed.; Oxford: Pergamon)
Macario, G., Markevitch, M., Giacintucci, S., et al. 2011, ApJ, 728, 82
Markevitch, M. 2006, in Proc. of The X-ray Universe 2005, ed. A. Wilson (Noordwijk: ESA), 723
Markevitch, M., & Vikhlinin, A. 2007, PhR, 443, 1
Mirakhor, M. S., Walker, S. A., & Runge, J. 2023, MNRAS, 522, 2105
Nurgaliev, D., McDonald, M., Benson, B. A., et al. 2017, ApJ, 841, 5
Ogrean, G. A., Brüggen, M., van Weeren, R., et al. 2014, MNRAS, 440, 3416

Owers, M. S., Nulsen, P. E. J., Couch, W. J., et al. 2014, ApJ, 780, 163
Owers, M. S., Randall, S. W., Nulsen, P. E. J., et al. 2011, ApJ, 728, 27
Piffaretti, R., Arnaud, M., Pratt, G. W., Pointecouteau, E., & Melin, J. B. 2011, A&A, 534, A109
Plagge, T., Benson, B. A., Ade, P. A. R., et al. 2010, ApJ, 716, 1118
Planck Collaboration, Ade, P. A. R., Aghanim, N., et al. 2016, A&A, 594, A13
Raja, R., Rahaman, M., Datta, A., et al. 2020, MNRAS, 493, L28
Richard, J., Patricio, V., Martinez, J., et al. 2015, MNRAS, 446, L16
Russell, H. R., McNamara, B. R., Sanders, J. S., et al. 2012, MNRAS, 423, 236
Russell, H. R., Nulsen, P. E. J., Caprioli, D., et al. 2022, MNRAS, 514, 1477
Russell, H. R., Sanders, J. S., Fabian, A. C., et al. 2010, MNRAS, 406, 1721
Sanders, J. S. 2006, MNRAS, 371, 829
Sanders, J. S., Fabian, A. C., Russell, H. R., Walker, S. A., & Blundell, K. M. 2016, MNRAS, 460, 1898
Sarazin, C. L. 1986, RvMP, 58, 1
Sarazin, C. L. 2002, in Merging Processes in Galaxy Clusters, ed. L. Feretti, I. M. Gioia, & G. Giovannini (Dordrecht: Kluwer), 1
Sarazin, C. L. 2008, in A Pan-Chromatic View of Clusters of Galaxies and the Large-Scale Structure, Vol. 740, ed. M. Large-Scale, O. L. ópez-Cruz, & D. Hughes (Dordrecht: Springer), 24
Sarkar, A., Randall, S., Su, Y., et al. 2022, ApJL, 935, L23
Takizawa, M. 1999, ApJ, 520, 514
Walker, S. A., Sanders, J. S., & Fabian, A. C. 2016, MNRAS, 461, 684
Wang, Q. H. S., Giacintucci, S., & Markevitch, M. 2018, ApJ, 856, 162
Williamson, R., Benson, B. A., High, F. W., et al. 2011, ApJ, 738, 139
ZuHone, J., & Su, Y. 2022, in Handbook of X-ray and Gamma-ray Astrophysics, ed. C. Bambi & A. Santangelo (Berlin: Springer), 93